Water Resources Research

RESEARCH ARTICLE
10.1029/2019WR026581

Key Points:
- Without any upscaling or homogenization, the fractures are explicitly represented to be of true finite volume
- The approach treats the fractured reservoir as a whole, which consists of fracture and matrix blocks with locally homogeneous properties
- The mess-free semianalytical solution based on BEM is flexible to capture the details of flow exchange between the matrix and fracture

Correspondence to:
L. Wang,
wanglei1986sp@foxmail.com

Citation:
Luo, W., Wang, J., Wang, L., & Zhou, Y. (2020). An alternative BEM for simulating the flow behavior of a leaky confined fractured aquifer with the use of the semianalytical approach. *Water Resources Research*, *56*, e2019WR026581. https://doi.org/10.1029/2019WR026581

Received 27 OCT 2019
Accepted 3 MAR 2020
Accepted article online 4 MAR 2020

An Alternative BEM for Simulating the Flow Behavior of a Leaky Confined Fractured Aquifer With the Use of the Semianalytical Approach

Wanjing Luo[1], Junlei Wang[2], Lei Wang[3], and Yingfang Zhou[4]

[1]China University of Geosciences, Beijing, China, [2]PetroChina Research Institute of Petroleum Exploration and Development, Beijing, China, [3]China University of Geosciences, Wuhan, China, [4]University of Aberdeen, Aberdeen, UK

Abstract This study developed an alternative boundary element method (BEM) to simulate the transient flow behavior of groundwater induced by well extraction in a confined fractured aquifer containing a network of discrete or connected fractures. The matrix flow, network-fracture flow, and matrix-fracture fluid exchange were considered. The aquifer was treated as a heterogeneous whole that consisted of fracture and matrix blocks with locally homogeneous hydraulic properties. The fractures were explicitly represented to be of true finite volume rather than nonrepresentational line sources. A semianalytical solution was developed based on the theory of a BEM in the Laplace transform domain, but the analytical Green's function was used for the bounded domain rather than the free-space Green's function in a conventional BEM. Case studies were presented in order to investigate the flow exchange behavior between the matrix and fractures and the corresponding transient drawdown response. The results showed that (1) exchange flux distribution calculated with the classical infinitesimal fracture model was consistent with the difference of the normal drawdown derivative values on both sides of the fracture body in our model. (2) When the well was in the matrix, the fractures acted as both highly conductive conduits and leaky faults, and the drawdown derivative behaviors resembled the characteristics of a dual-porosity reservoir model. (3) When the well was in the network fracture and when the volume of fracture was of the same order of magnitude as the matrix, the drawdown derivative might exhibit the look-alike behavior of a dual-porosity model.

1. Introduction

All geological settings/rocks are fractured with a variety of scales to some extent. There are a great number of fractures in certain types of geological formations, such as naturally fractured reservoirs, fractured low-permeability rocks, and fractured confined aquifers (Jiang et al., 2013; Kuhlman et al., 2015; Marechal & Dewandel, 2004; Sedghi & Zhan, 2019; Smith & Schwartz, 1984). As highly efficient flow channels, fractures play an important role in conducting fluids throughout the groundwater system into a wellbore. Matrixes and fractures have different scales, each being assigned to different geometrical properties. The general equation for describing the fluid flow in fractured porous media is given as a quasi-Laplace equation:

$$\nabla\left(k\left(\vec{r}\right)\cdot\nabla p\right)=\varphi\mu c\frac{\partial p}{\partial t}, \tag{1}$$

where the permeability k is likely to have strong nonuniformity. This flow model can be adopted to describe both groundwater and hydrocarbon flows based on the flowing analogy between an aquifer and reservoirs. The modeling of fractured aquifers and reservoirs is a long-standing research topic. Many studies have dealt with groundwater flows in discrete fracture system in unconfined aquifers and the interactions between aquifers and fractures. These studies have generally solved the complicated model with a numerical approach. For the mesh-reliant numerical method, the exchange rate between a fracture and matrix cells in two dimensions is evaluated by

$$\left(Q_x\right)_{i+0.5,j}=-Tx_{i+0.5,j}\frac{p_{i+1,j}-p_{i,j}}{\Delta x}\ \text{and}\ \left(Q_y\right)_{i,j+0.5}=-Ty_{i,j+0.5}\frac{p_{i,j+1}-p_{i,j}}{\Delta y}, \tag{2}$$

and $Tx_{\mathrm{i}\,+\,1/2,\mathrm{j}}$ and $Ty_{\mathrm{i,j}\,+\,1/2}$ are the internodal transmissivities. Internodal transmissivity is calculated with

the use of various averaging methods, such as a harmonic mean, arithmetical mean, or exponentially weighted mean. It should be emphasized that these algorithmic errors increase with the increase of the permeability heterogeneity. To capture the strong heterogeneity between a fracture and a matrix, various techniques have been presented to subdivide the grids, such as local refined gridding, unstructured gridding, and an embedded discrete fracture model (EDFM) (Karimi-Fard & Durlofsky, 2016; Xu et al., 2017, 2019; Zidane & Firoozabadi, 2014). A flexible finite element Galerkin method has also been used to describe the transient flux of fluid from a matrix into fractures in a confined leaky aquifer (Duguid & Lee, 1977). However, obtaining accurate transmissibility by computing the irregular connections between fracture segments is still a huge challenge. Considering the high computational burden and the great difficulties in describing geometrical complexity, mess-free analytical and semianalytical methods have been developed as an alternative to numerical simulation methods.

The first dual-porosity continuum model was developed by Barenblatt et al. (1960) and Warren and Root (1963). In the double-porosity model, a matrix and a fracture are considered to be two porosity types that coexist at the same spatial location, and the mass transfers between those two porosity types are coupled through a transfer function. Afterwards, various semianalytical solutions in the hydrogeology literature were presented for the interpretation of the transient drawdown behaviors in all types of wells (e.g., vertical, horizontal, partially penetrating) and aquifer configurations (e.g., fractured wedge-shaped and unconfined-fractured aquifers). Moench (1984) determined the analytical solutions of the flow to a well in a double-porosity groundwater reservoir with consideration of a thin layer of low permeability at the fracture-matrix block interface. Park and Zhan (2003) obtained the analytical solution of the groundwater flow to a horizontal well in fractured confined, leaky, and unconfined aquifers by considering the interporosity flux based on a spherically approximated matrix block. Kuhlman et al. (2015) presented a multiporosity extension for double- and triple-porosity models for the flow modeling in fractured rock reservoirs, whose models included a fracture continuum and an overlapping distribution of multiple rock matrix continua. Sedghi et al. (2018) adopted the dual-porosity concept to develop a semianalytical solution for modeling the interporosity flow in an unconfined fractured aquifer system. Wang and Xue (2018) presented a semianalytical model for a pumping test in irregularly shaped double-porosity aquifers using the novel boundary element method (BEM). Sedghi and Zhan (2019) presented the analytical solutions of groundwater dynamics in an unconfined dual-porosity aquifer subjected to a time-dependent areal recharge. Over the years, for the continuum model, more focus has been put on characterizing the transient behavior of the interporosity fluid exchange between a matrix and fractures.

In fact, the continuum model is a spatial averaging approach based on the representative elementary volume (REV) concept (Kuchuk & Biryukov, 2014; Ren et al., 2017). The model is justified only when a formation contains a dense network of highly interconnected fractures, where a fractured formation would behave more like a continuum. In other words, it is an equivalent model, and the effect of fractures is averaged out over the continuum region. For a discretely fractured formation that is more realistic in nature, the characteristic volume considered in the continuum model is generally greater than the REV of the discretely fractured formation, so it is very difficult for the continuum model to capture the flow behavior of this type of fractured formation no matter how many levels of continuum are used. As a result, the discrete fracture network (DFN) model was developed to improve the continuum model. In principle, the DFN model is a rigorous "discontinuum" approach that could describe the anisotropy in the permeability of a fractured rock mass. The geological and hydraulic characteristics of each fracture are explicitly considered throughout the formation. Smith and Schwartz (1984) developed a modeling technique to investigate how fracture geometry influences the velocity distributions and mass transport within a DFN with two orthogonal fracture sets. Based on a field-scale representation of the hydraulic fracture properties from the Sellafield area, Leung et al. (2012) simulated the steady-state constant density groundwater flow through a two-dimensional fracture network using a DFN model. Jiang et al. (2013) used the variational inequality (VI) theory to solve the free-surface unconfined seepage flow in a percolating fracture network. Fang and Zhu (2018) simulated groundwater flow using an overlying unconfined aquifer, an underlying DFN, and their exchange. Liu et al. (2018) presented a numerical study on the geometrical and hydraulic properties of a three-dimensional intersected fracture model, and then the evaluations of the aperture distributions, flow channels and equivalent permeability of fractures were studied. However, these previous studies assumed that the rock matrix was impermeable and the groundwater could only flow through the DFN.

In fact, the contribution of the matrix flow cannot be neglected in many types of leaky fractured aquifers (Berkowitz, 2002; Marechal & Dewandel, 2004). Roubinet et al. (2012) developed a semianalytical solution for the transport of conservative solutes in a single fracture. Houseworth et al. (2013) derived an analytical model for solute transport that used a water-saturated single fracture in a permeable rock matrix. Although these semianalytical models could consider the fluid transfer between a matrix rock and each individual fracture, more emphasis was placed on the consideration of flow mechanisms in an individual fracture and matrix. In addition to numerical approaches, few semianalytical approaches could account for the geometrical complexity of a DFN and the matrix flow along with fracture flow.

Due to the flexibility in accounting for a fracture-matrix fluid transfer and the interconnection of a fracture network, the source/sink-function methods suggested by Cinco-Ley et al. (1976, 1978) have been widely applied to model the transient flow and transport in both the fractures and the surrounding rock matrixes in hydrogeology and petroleum engineering. There are two basic assumptions:

i A fracture is regarded as a (zero-width) line source, which is obtained by the spatial integration of the continuous point source function.
ii Fluid enters the fracture at a rate $q(x,t)$ per unit of fracture length, and the flow across the fracture edge and the fluid compressibility are generally negligible.

Using the Fredholm integral equation, Izadi and Yildiz (2009) investigated the transient flow behavior of a vertical well near randomly distributed discrete fractures. Luo et al. (2018) presented a semianalytical method for calculating the pseudo-steady-state productivity index of a vertical well near discrete fractures. When fractures connect with each other in a network configuration, the mass exchange of fluid flow in the fracture-fracture nodes must be considered. Zhou et al. (2013) used the principle of mass balance to establish a constraint condition for each of the intersection points that stated that the inflow must equate to the outflow. Jia et al. (2016, 2017) introduced a star-delta transformation to automatically judge the flow direction at an intersection point with a fracture network. Luo et al. (2019) established a Z-fold fracture model to describe the fluid flow in a fracture unit (consisting of two connection nodes and one fracture segment) based on the Luo-Tang wing model (Luo & Tang, 2014).

It should be noted that the DFN models mentioned above were established based on the assumption that the volume of a fracture would be neglected compared with the volume of the surrounding matrix. In other words, a fracture is a primary singularity of the flux density (i.e., the flux divergence on the edges of a fracture) in the mathematical context. Under this assumption, there are two inconsistent phenomena with the reservoir simulation: (i) For extra-low contrast where the conductivities of the fractures and matrix are close enough, a well cannot exhibit the pressure behavior of a homogeneous medium as expected. (ii) For a continuous fractured reservoir in which fractures are in a network and communicate with each other throughout the system, the case of a well located within a fracture network cannot resemble the pressure response of the Warren and Root dual-porosity geological model (Biryukov & Kuchuk, 2012; Dejam et al., 2018; Kuchuk & Biryukov, 2014).

Based on the theory of a BEM (Jia et al., 2017; Wang & Xue, 2018) and Green's function (Fen & Yeh, 2012; Wang et al., 2017), an efficient approach was developed in this work to account for the finite volume of fractures and to relax the assumption of infinitesimal fracture volume. This paper is organized as follows. The model establishment and a semianalytical solution are introduced in section 2. By performing a constant-rate pumping test in a fractured confined aquifer, the characteristics of groundwater flow behavior and corresponding drawdown response for the pumping well were investigated, as described in section 3. The discussions of the contradictory phenomena mentioned above are described in section 4. The conclusions are described in section 5.

2. Methodology

2.1. Mathematical Model

In this study, the model was assumed to be two-dimensional. We assumed that the pumping well fully penetrated the aquifer and that the groundwater flow was essentially horizontal. The vertical flow was not considered. We assumed that the aquifer was a horizontal, isotropic, and finite-extended confined aquifer with a uniform thickness. Additionally, a single-phase slightly compressible fluid flow was considered.

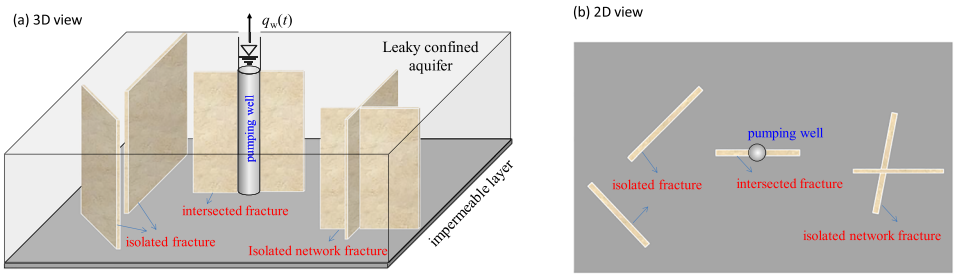

Figure 1. Schematic presentation of the confined fractured aquifer.

Figure 1 shows a schematic representation for the model describing the groundwater flow in a confined aquifer with a set of fractures. The aperture of each fracture did not vary along the fracture length. Between the matrix and the fractures, the groundwater in the aquifer could flow from the network fractures to the matrix or from the network fractures to the matrix, that is, fluid exchange. Finally, the extracted groundwater was released from the aquifer elastic storage to a pumping well. In this study, only large-scale fractures were explicitly represented, and small-scale fractures were considered as the continuum. As shown in Figure 1, all types of fracture configuration were presented:

- The isolated fracture was identified as the fracture with no interconnection in the fracture.
- The intersected fracture was identified as the fracture directly connected to the pumping well.
- The network fracture was identified as the fracture with an intersection. If the network contained a fracture directly connected to the pumping well, the network was denoted as a connected network; otherwise, it was denoted as an isolated network.

The confined fractured aquifer was further divided into a set of blocks, as shown in Figure 2. In the figure, the white block represents the fracture block, which was surrounded by several matrix blocks. Each block had locally homogeneous properties.

The general two-dimensional equations describing the drawdown due to well pumping in the matrix or the fracture block could be expressed as

$$\begin{cases} \dfrac{\partial^2 s_\alpha(M,\,t)}{\partial x^2}+\dfrac{\partial^2 s_\alpha(M,\,t)}{\partial y^2}+\dfrac{1}{T_\alpha}F_{w\alpha}(M,\,t)=\dfrac{S_\alpha \partial s_\alpha(M,\,t)}{T_\alpha \quad \partial t} & M\in\Omega_\alpha,\quad t>0 \\ s_\alpha(M,\,t)=0 \quad M\in\Omega_\alpha,\quad t=0 & \\ \dfrac{\partial s_\alpha(M,\,t)}{\partial n_B}=\dfrac{1}{T_\alpha}q_B^\alpha(M,\,t) & M\in\Gamma_{B\alpha},\quad t=0 \end{cases}, \tag{3}$$

where the subscript α represents the matrix (m) and the fracture (f) block. $\Gamma_{B\alpha}$ is the outer boundary of the αth block, and the non-homogeneous term $F_{w\alpha}$ is the function on the inner boundary. In equation 3, s_α is the aquifer drawdown representing the change of the hydraulic head due to pumping and $M = (x,y)$ is a Cartesian coordinate in local block system.

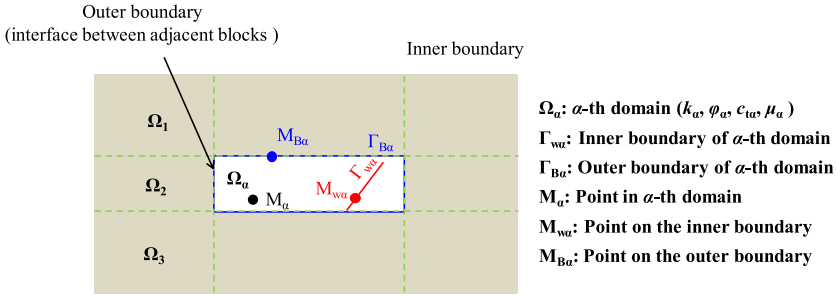

Figure 2. Schematic of the confined aquifer containing a finite-width fracture.

In addition, $q_B^{\alpha}(M,\ t)$ was the flow exchange rate on the outer boundary. $F_{w\alpha}(M,t)$ was the production function caused by fluid withdrawal, which could be represented by a line or a point source. If there was a pumping well, $F_{w\alpha}(M,t) \neq 0$; otherwise, $F_{w\alpha}(M,t) = 0$. It was expressed by different functions, which were given as

$$F_{w\alpha}(M,\ t) = \begin{cases} \int_0^{L_f} q_{wf}(u,\ t)\delta(x - x_{of} - u\cos\theta)\delta\left(y - y_{of} - u\sin\theta\right)du, & \text{for line source} \\ q_{wv}(t)\delta(x - x_w)\delta(y - y_w), & \text{for point source} \end{cases}, \tag{4}$$

where q_{wf} is the pumping rate per unit along the line source, q_{wv} is pumping rate per unit of the well, L_f is the fracture length, (x_{of}, y_{of}) represents the Cartesian coordinate of the fracture tip, θ is the azimuth of fracture, (x_w,y_w) is a Cartesian coordinate of the pumping well, and the Dirac delta function is defined as

$$\delta(M - M') = \begin{cases} \infty,\ M = M' \\ 0,\ M \neq M' \end{cases}.$$

As shown in Figure 2, the interface between two adjacent blocks Ω_α and $\Omega_{\alpha+1}$ was defined as $\Gamma_{\alpha,\alpha+1}$, and flow across the interface between two blocks satisfied the continuities of drawdown and flux:

$$\begin{cases} s_\alpha = s_{\alpha+1} \\ T_\alpha \dfrac{\partial s_\alpha}{\partial n_B} = T_{\alpha+1} \dfrac{\partial s_{\alpha+1}}{\partial n_B} \text{ at } \Gamma_{\alpha,\alpha+1}. \end{cases} \tag{5}$$

It should be noted that $\Gamma_{\alpha,\alpha+1} = \Gamma_{B\alpha} = \Gamma_{B\alpha+1}$.

For the special case in which the fracture was assumed to have a one-dimensionl flow pattern, equation 3 was reduced to the following equation:

$$\frac{\partial^2 s_f}{\partial x^2} + \frac{T_f w_f}{T_m}\left[\frac{\partial s_f}{\partial y}\right]_{\Gamma_{m,f}} = \frac{S_f}{T_f}\frac{\partial s_f}{\partial t} - \frac{1}{T_f}F_f(M,\ t), \qquad \left[\frac{\partial s_f}{\partial x}\right]_{\Gamma_{m,f}} = 0 \text{ on the fracture edge}, \tag{6}$$

where w_f is fracture width, (x,y) is the local Cartesian coordinate system in the fracture block, x is the tangential direction, and y is the direction normal to the fracture. $\Gamma_{m,f}$ indicates the fracture-matrix interface. When the fracture width was approximately zero-width, the exchange rate between fracture and the matrix was satisfied as

$$\left[\frac{\partial s_f}{\partial y}\right]_{\Gamma_{m,f}} = \lim_{y\to 0^+}\left[\frac{\partial s_f}{\partial y}\right] - \lim_{y\to 0^-}\left[\frac{\partial s_f}{\partial y}\right]. \tag{7}$$

After substituting equation 7 into equation 6, the right-hand side of equation 6 was consistent with the expression of Cinco-Ley et al. (1978), which was based on the zero-width assumption. Thus, Cinco-Ley's fracture model is a special form of equation 3.

2.2. Boundary Element Solution for the Substructure

The nonhomogeneous equation could be solved with the use of the BEM. After eliminating the nonhomogeneous terms in equation 3, the auxiliary equations of Green's function were established:

$$\begin{cases} \nabla^2 G_\alpha(M,\ M',\ t,\ \tau) + \dfrac{1}{T_\alpha}\delta(M - M')\delta(t - \tau) = 0, & (M,\ M') \in \Omega_\alpha,\quad t > \tau \\ G_\alpha(M,\ M',\ t,\ \tau) = 0, & (M,\ M') \in \Omega_\alpha,\quad t < \tau \\ \dfrac{\partial G_\alpha}{\partial n_B} = 0, & (M,\ M') \in \Gamma_{B\alpha},\quad t > \tau \end{cases}, \tag{8}$$

where G is Green's function, and the Laplace operators are given as

$$\nabla^2 = \frac{\partial^2}{\partial x^2} + \frac{\partial^2}{\partial y^2} - \frac{S_\alpha}{T_\alpha}\frac{\partial}{\partial t},\ \nabla'^2 = \frac{\partial^2}{\partial x'^2} + \frac{\partial^2}{\partial y'^2} - \frac{S_\alpha}{T_\alpha}\frac{\partial}{\partial \tau}. \tag{9}$$

$G_\alpha(M,M',t,\tau)$ is defined as the drawdown at (M,t) caused by a source of unit strength at (M',τ), and n_B is the outward normal direction of the boundary surface. Based on the reciprocity theorem in Green's function method (Wang & Xue, 2018) and Green's secondary identity, the expression gives

$$\iiint_{\Omega_\alpha} \left(s_\alpha \nabla'^2 G_\alpha - G_\alpha \nabla'^2 s_\alpha\right) dM = \oint_{\Gamma_\alpha} \left(s_\alpha \frac{\partial G_\alpha}{\partial n_B} - G_\alpha \frac{\partial s_\alpha}{\partial n_B}\right)_{M\in\Gamma_\alpha} dM, \tag{10}$$

where the boundary Γ_α includes the inner and outer boundaries, as follows: $\Gamma_\alpha = \Gamma_{B\ \alpha} + \Gamma_{w\ \alpha}$.

By substituting equations 3 and 8 into equation 10, an explicit pressure solution was produced:

$$\begin{aligned} s_\alpha(M,\ t) = &-\frac{T_\alpha}{S_\alpha}\int_0^t d\tau \oint_{\Gamma_{B\alpha}} \left[G_\alpha(M,M',t-\tau)\frac{\partial s_\alpha(M',\tau)}{\partial n_B} - s_\alpha(M',\tau)\frac{\partial G_\alpha(M,M',t-\tau)}{\partial n_B}\right]_{M'\in\Gamma_{B\alpha}} dM' \\ &+ \frac{1}{S_\alpha}\int_0^t d\tau \iiint_{\Omega_\alpha} F_{w\alpha}(M,\tau) G_\alpha(M,\ M',\ t-\tau) dM'. \end{aligned} \tag{11}$$

It should be noted that the main difference from the conventional BEM was that we used the Green's function for the bounded domain (constrained by the boundary condition in equation 8) rather than the conventional free-space Green's function. Since the Green's function satisfied the Neumann boundary condition, the normal derivative of the Green function was equal to zero, $\partial G/\partial n_B = 0$. Using Darcy's law to represent the normal derivatives of pressure on the boundary $\left[q_B^\alpha = -T_\alpha(\partial s_\alpha/\partial n_B)\right]$, equation 11 could be rewritten as

$$s_\alpha(M,\ t) = \frac{1}{S_\alpha}\int_0^t d\tau \oint_{\Gamma_{B\alpha}} \left[q_B^\alpha G_\alpha(M,M',t-\tau)\right]_{M'\in\Gamma_{B\alpha}} dM' + \frac{1}{S_\alpha}\int_0^t d\tau \iiint_{\Omega_\alpha} F_{w\alpha}(M,\tau) G_\alpha(M,\ M',\ t-\tau) dM'. \tag{12}$$

The solution of equation 12 was dependent on the knowledge of the flow exchange on the interface boundary (i.e., the outer boundary), while the exchange was an unknown priori. Thus, these boundary quantities needed to be determined beforehand. To do this, the outer boundary was discretized into a set of linear segments (j = 1,2,3 ..., N). The flow exchange on each segment was assumed to be the uniform flux.

Due to the analogy of the fluid flow between the reservoir and the aquifer, we used the definitions of the dimensionless variables, as follows:

$$s_D^\alpha = \underbrace{\frac{2\pi k_{\mathrm{ref}} h}{q_w \mu B}(p_0 - p_\alpha)}_{\text{reservoirs}} = \underbrace{\frac{2\pi T_{\mathrm{ref}}}{q_w} s_\alpha}_{\text{aquifers}},\ t_D = \underbrace{\frac{k_{\mathrm{ref}} t}{(\varphi c \mu)_{\mathrm{ref}} L_{\mathrm{ref}}^2}}_{\text{reservoirs}} = \underbrace{\frac{T_{\mathrm{ref}} t}{S_{\mathrm{ref}} L_{\mathrm{ref}}^2}}_{\text{aquifers}},\ \varsigma_D = \frac{\varsigma}{L_{\mathrm{ref}}},\ q_{\xi D} = \frac{q_\xi L_{\mathrm{ref}}}{q_w},\ G_D = 2\pi L_{\mathrm{ref}}^2 G.$$

The subscript $\xi = B$ and wf, the subscript D represents a dimensionless symbol, and the subscript ref represents the reference variable. t is the time, B is the volume factor, h is the aquifer thickness, μ is the fluid viscosity, q_w is the pumping rate of the surface, φ is the matrix porosity, c_t is the total compression factor, p is the pressure, and p_0 is the initial pressure. k is the reference permeability, L is the reference length, T is the transmissivity, and S is the storage coefficient. With the definition of the above dimensionless variables and discretization, equation 12 became the following expression:

$$s_D^\alpha(M_D,t_D) = \frac{T_{ref}}{T_\alpha}\left\{\sum_{j=1}^{N}\int_0^{t_D} q_{BDj}^\alpha(\tau_D)\overline{S}_{BDj}^\alpha(M_D,t_D-\tau_D)d\tau_D + \int_0^{t_D} d\tau_D \iiint_{\Omega_{D\alpha}} F_{D\alpha}(M_D,\tau_D) G_{D\alpha}(M_D,M_D',t_D-\tau_D)\right) dM_D'\}, \tag{13}$$

where the linear source function for the jth linear segment on the outer boundary is

$$\overline{S}_{BDj}^\alpha(M_D,t_D-\tau_D) = \frac{T_{D\alpha}}{S_{D\alpha}}\int_{\Gamma_{BD\alpha,j}} \left[G_{D\alpha}\left(M_D,M_D',t_D-\tau_D\right)\right]_{M_D'\in\Gamma_{BD\alpha}} dM_D'. \tag{14}$$

By applying the Laplace transformation and the convolution-integral operation to equations 13 and 14, the following expression was produced:

$$\widetilde{s}_D^{\alpha}(M_D) = \frac{1}{T_{D\alpha}}\left[\underbrace{\sum_{j=1}^{N}\widetilde{q}_{BDj}^{\alpha}(\nu)\widetilde{\overline{S}}_{BDj}^{\alpha}(M_D,\nu)}_{\text{source function on outer boundary}} + \underbrace{\oint\!\!\!\!\!\!\int_{\Omega_{D\alpha}}\widetilde{F}_{wD\alpha}(M_D,\nu)\widetilde{G}_{D\alpha}\left(M_D,M_D^{'},\nu\right)dM_D^{'}}_{\text{source function on inner boundary}}\right], \tag{15}$$

where ν is the dimensionless time t_D transformed into the Laplace space, and superscript "~" indicates the Laplace-transformed variables. Correspondingly, the source function for the inner boundary could be determined by substituting equation 4 into the secondary term on the right-hand side of equation 15 and then using the Fourier cosine transformation. Its expression was equivalent to the conventional analytical solution in a rectangular medium with impermeable boundaries (Ozkan & Raghavan, 1991).

Equation 15 was the building block of our solution method. It required the fundamental Green's function on the inner and outer boundaries of the domain. The detailed derivations can be seen in Appendix A. It should be emphasized that the computational consideration for Green's function was also an important contribution in our study.

2.3. Coupled Solution

To demonstrate the coupling of multiple blocks, we took the model shown in Figure 3 as an example. The example included four rectangular blocks, and each block contained two outer boundaries (denoted by the green line) and an inner boundary (the red line). Thus, the pressure drop on the center of the jth line segment within the αth block was expressed as

$$\widetilde{s}_D^{\alpha}(M_{Dj}) = \frac{1}{T_{D\alpha}}\left[\sum_{n=1}^{2}\sum_{i=1}^{N_B}\widetilde{q}_{BDn,i}^{\alpha}\,\widetilde{\overline{S}}_{BDn,i}^{\alpha}(M_{Dj}) + \sum_{i=1}^{N_w}\widetilde{q}_{wD1,i}^{\alpha}\widetilde{\overline{S}}_{wD1,i}^{\alpha}(M_{Dj})\right]. \tag{16}$$

q_{wD} and q_{BD} represent the rate strengths for the line segments on the inner and outer boundaries, S_{wD} is the dimensionless source function on the inner boundary, and S_{BD} is the dimensionless source function on the outer boundary.

Writing equation 16 at the center of all of the inner and outer boundaries yielded the following set of linear equations in unknowns, which were given by

$$\begin{cases}\widetilde{s}_{BDm,j}^{\alpha} = \dfrac{1}{T_{D\alpha}}\left[\displaystyle\sum_{n=1}^{2}\sum_{i=1}^{N_B}\widetilde{q}_{BDn,i}^{\alpha}\,\widetilde{\overline{S}}_{BD(m,j;n,i)}^{\alpha} + \sum_{i=1}^{N_w}\widetilde{q}_{wD1,i}^{\alpha}\widetilde{\overline{S}}_{wD(m,j;1,i)}^{\alpha}\right] \\ \widetilde{s}_{wDm,j}^{\alpha} = \dfrac{1}{T_{D\alpha}}\left[\displaystyle\sum_{n=1}^{2}\sum_{i=1}^{N_B}\widetilde{q}_{BDn,i}^{\alpha}\,\widetilde{\overline{S}}_{BD[m,j;n,i]}^{\alpha} + \sum_{i=1}^{N_w}\widetilde{q}_{wD1,i}^{\alpha}\widetilde{\overline{S}}_{wD[m,j;1,i]}^{\alpha}\right]\end{cases}, \tag{17}$$

where $(m,j;n,i)$ indicates the drawdown of the jth segment on the mth outer boundary, while $[m,j;n,i]$ indicates the drawdown of the jth segment on the mth inner boundary.

We assumed that $N_B = 2$ and $N_w = 2$. Based on the continuity conditions of the pressure and flux at the outer boundary, adjacent blocks were coupled together to form a linear system, which could be expressed in matrix-vector form:

$$\begin{pmatrix}\mathbf{A}_1 & \mathbf{A}_2 \\ \mathbf{A}_3 & \mathbf{A}_4\end{pmatrix}\cdot\left(\vec{X}_1\,\vec{X}_2\right) = \left(\vec{B}_1\,\vec{B}_2\right). \tag{18}$$

The unknown vectors had the following components:

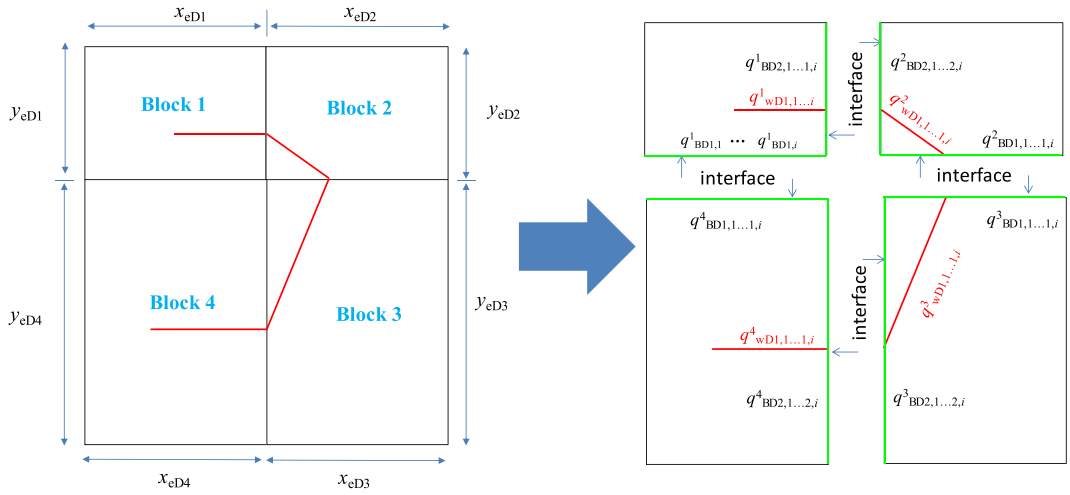

Figure 3. Discretization scheme to demonstrate the coupling of four blocks.

$$\vec{X}_1^T = \left(\underbrace{\tilde{q}^1_{BD1,1}, \tilde{q}^1_{BD1,2}, \tilde{q}^1_{BD2,1}}, \tilde{q}^1_{BD2,2}, \tilde{q}^1_{wD1,1}, \tilde{q}^1_{wD1,2\text{Block1}} \cdots \underbrace{\tilde{q}^4_{BD1,1}, \tilde{q}^4_{BD1,2}, \tilde{q}^4_{BD2,1}}, \tilde{q}^4_{BD2,2}, \tilde{q}^4_{wD1,1}, \tilde{q}^4_{wD1,2\text{Block4}} \right), \tag{19}$$

and

$$\vec{X}_2^T = \left(\underbrace{\tilde{s}^1_{BD1,1}, \tilde{s}^1_{BD1,2}, \tilde{s}^1_{BD2,1}}, \tilde{s}^1_{BD2,2}, \tilde{s}^1_{wD1,1}, \tilde{s}^1_{wD1,2\text{Block1}} \cdots \underbrace{\tilde{s}^4_{BD1,1}, \tilde{s}^4_{BD1,2}, \tilde{s}^4_{BD2,1}}, \tilde{s}^4_{BD2,2}, \tilde{s}^4_{wD1,1}, \tilde{s}^4_{wD1,2\text{Block4}} \right). \tag{20}$$

Equation 18 treated the domain of interest as a whole. The boundary element discretization rendered the domain as a mess-free semianalytical solution, rather than discretizing it into small grid blocks and time steps as a numerical finite-difference method. The details for the coefficient matrix structure **A** and the known vector ***B*** in equation 18 are provided in Appendix B.

The equations could be solved by the Gauss elimination method in the Laplace transformation domain. The Stehfest numerical inversion algorithm (Stehfest, 1970) was used to obtain the solutions in the real-time domain. The solution of the linear equations provided the fluxes and drawdowns for the outer boundary and inner boundary segments. When compared with the numerical methods, the presented approach could compute the drawdown at any grid point and time with equation 16, and it took much less time to obtain the required results.

3. Results

In the following section of groundwater flow modeling, we discuss the transient response behavior of two benchmark cases based on semianalytical solutions. The first benchmark case showed a conceptual confined fractured aquifer as a base case. The second benchmark case provided a realistic example for investigating the applicability of the present model. It should be noted that when a pumping well was drilled in the confined fractured aquifer, there were only two possibilities: (i) The well did not intercept any fractures, that is, the well was in the matrix, and (ii) the well intersected a fracture.

3.1. Behavior of the Fracture-Matrix Fluid Exchange

3.1.1. Discretely Confined Fractured Aquifer

In this section, the term discretely confined fractured aquifer refers to an aquifer that contained an isolated or intersected fracture. The ratio of fracture width to the length was set to 0.001 (i.e., the fracture

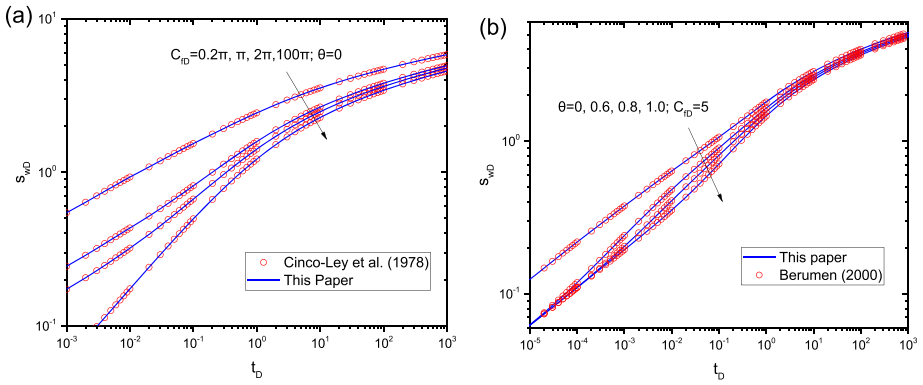

Figure 4. Comparison of our solution and the classical solution for (a) a symmetrically fractured well (Cinco-Ley et al., 1978) and (b) an asymmetrically fractured well (Berumen et al., 2000).

approximated the assumption of a zero-width volume), the fracture-matrix diffusivity ratio was 10^5 (i.e., the flow in the fracture was approximately incompressible), and the exchange across the fracture edge, which was given by $(\partial s_f/\partial x)|_\Gamma = 0$, was ignored. It should be noted that the fracture conductivity was defined as

$$C_{fD} = \frac{T_f w_f}{T_m L_{ref}}, \text{ where } L_{ref} = L_f/2. \tag{21}$$

As seen in Figure 4a, we compared the dimensionless drawdown solution for the case of the wellbore intersecting of a finite-conductivity fracture (Cinco-Ley et al., 1978) with our solution. The fracture asymmetry could be flexibly considered by altering the location of the wellbore in the fracture-block domain. Figure 4b compares our solutions with the solutions for an asymmetrically fractured well (Berumen et al., 2000). It was considered that for the symmetry of the fracture body in the direction normal to the fracture, at any location of the fracture face ($x_D \in \Gamma$), the flux density function given by Cinco-Ley et al. (1978) was equal to the difference of the normal pressure derivative values at both sides of the fracture:

$$q_{fD}(x_D) = \lim_{y_D \to 0^+} \left[\frac{\partial s_{fD}}{\partial y_D}\right]_\Gamma - \lim_{y_D \to 0^-} \left[\frac{\partial s_{fD}}{\partial y_D}\right]_\Gamma = 2 \lim_{y_D \to 0^+} \left[\frac{\partial s_{fD}}{\partial y_D}\right]_\Gamma = -2 \lim_{y_D \to 0^-} \left[\frac{\partial s_{fD}}{\partial y_D}\right]_\Gamma. \tag{22}$$

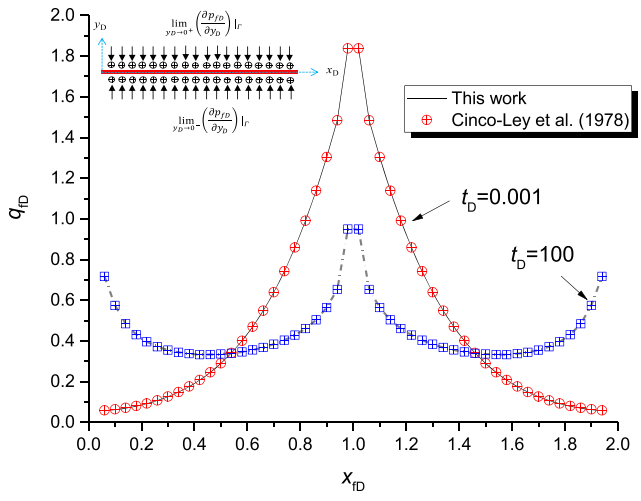

Figure 5. Flux distribution along the fracture calculated using equation 22 for the case of a wellbore-intersecting fracture ($C_{fD} = \pi$).

It should be noted that the exchange rate is a vector, where a positive value represents the outflow (or withdrawal) and a negative value represents the inflow (or injection). According to equation 22, Figure 5 shows the exchange flux distributions along the fracture for early and late time periods. The line plot indicates the calculated results from our model, and the scatter plot indicates the influx rate using Cinco-Ley's method. As seen from these two figures, our results matched very well with Cinco-Ley's method results.

For convenience, as shown in Figure 6a, the matrix that contained a vertical well was defined as the right-hand side (RHS) region, and the opposite matrix was defined as the left-hand side (LHS) region. Figure 6b shows that along the fracture surface in the LHS region, the fluids were always withdrawn from the matrix and then injected back into fracture body. The fracture face in the RHS received fluid from the matrix region far away from the vertical well. In the RHS region near the vertical well ($0.9 < x_{fD} < 1.1$), a mass of fluids within the fracture outflowed into the matrix, which was attributed to the withdrawal by the production well. According to the dimensionless pressure field shown in Figure 6c, the fracture was a combination of a conductive channel and a leaky fault.

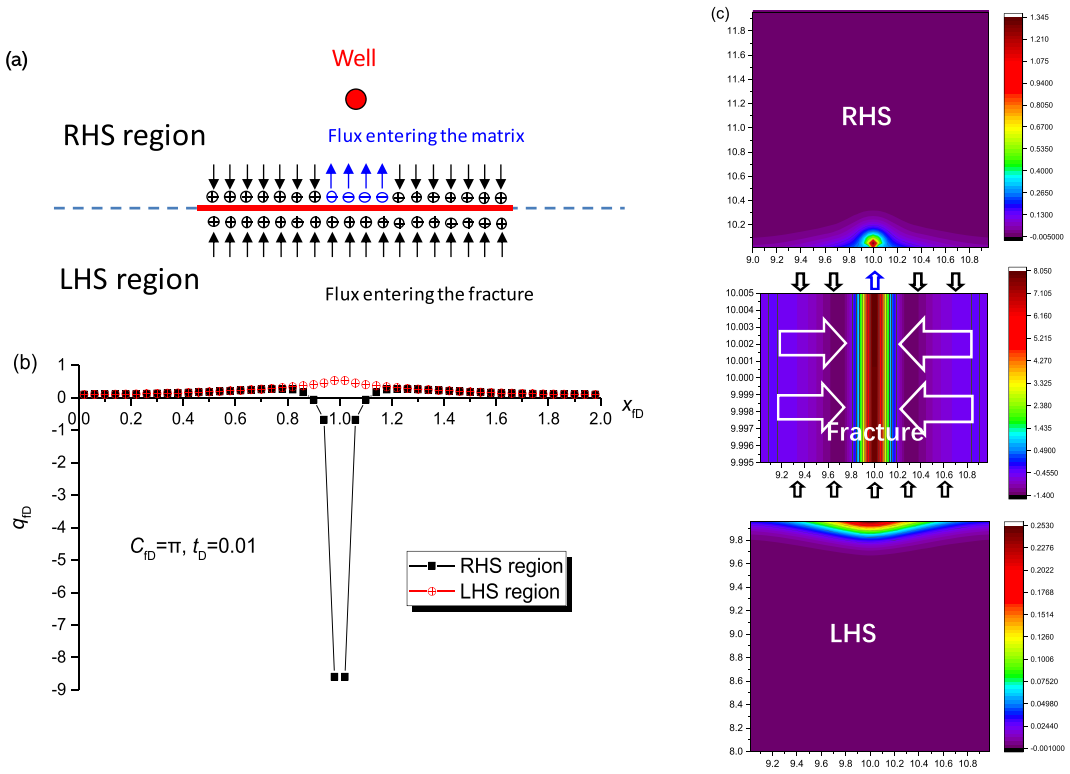

Figure 6. Flow behavior of an isolated fracture characterized by (a) the schematic for the flow exchanges between the fracture and the matrix, (b) flux distribution on the RHS and LHS of the fracture body, and (c) dimensionless drawdown field in both the fracture and the matrix.

The fluid passed through/across the leaky fault, which was described by the following equation (Biryukov & Kuchuk, 2012):

$$T_m \frac{\partial s^+}{\partial y} = T_m \frac{\partial s^-}{\partial y} = \frac{T_f}{w_f}(s^+ - s^-) \text{ in the region of } 9.8 < x_D < 10.2, \tag{23}$$

where s^+ and s^- are the hydraulic drawdowns on the RHS and LHS, respectively. In the other region, the fluids entered the fracture and they were then conducted through the fracture towards the leaky fault region.

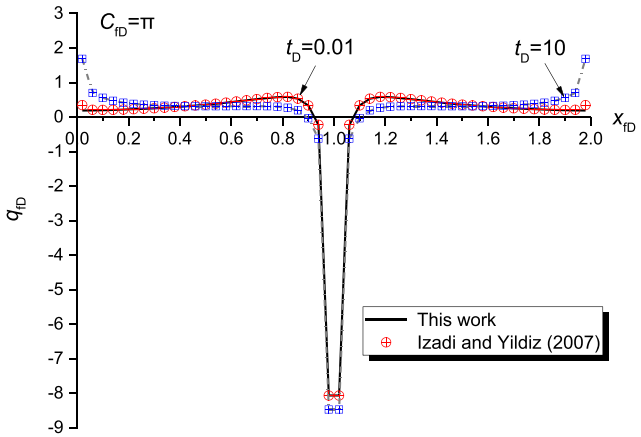

Figure 7. Flux distribution along the fracture calculated using equation 22 for the case of a wellbore near an isolated fracture.

Based on equation 22, Figure 7 compares the calculated exchange flux distribution with the Izadi and Yildiz (2009) solution (the fracture conductivity was considered). This showed that the fluids entered the fracture at the far end and left the fracture at the region close to the wellbore.

3.1.2. Continuously ConfinedFractured Aquifer

As described in this section, the fractures created a network and communicated with each other throughout the system. The matrix blocks were uniformly distributed, and fractures were orthogonal and of uniform conductivity. The size of the network-fractured zone was finite, and the aquifer resided in a homogeneous matrix beyond the extent of fractured zone. In this section, we provide two examples according to the well location: in a matrix block and an intersecting fracture. Figure 8 shows that the solutions from our model agreed very well with the numerical simulation (the accurate numerical solutions were generated with the use of the technique of the local gridding refine [LGR] presented by Berumen et al., 2000). The computation times for our model and the numerical method were

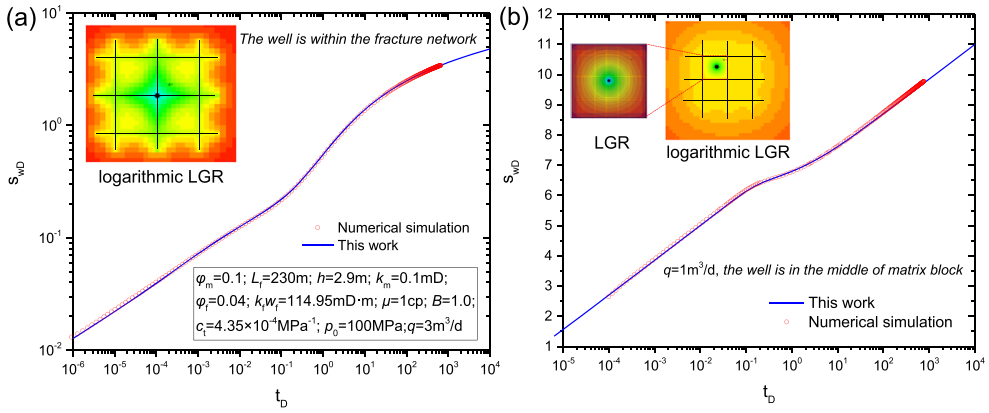

Figure 8. Comparison of our model and the numerical simulations of a continuously fractured confined aquifer for the case of the well (a) in the fracture network and (b) in the matrix block.

compared based on of the same hardware platform. For the above simulations, the computation times were 30.6 and 52.5 s in this study and in the numerical model, respectively. The advantage of the computation performance of this model was not demonstrated because of the number of fractures (six fractures) and network configuration (orthogonal). As a result, the improvement of the computation speed was not remarkable. The computation cost could be efficiently reduced by using the case with a complex geometry for the network fractures.

It should be noted that when the fracture and matrix storativity had the same order of magnitude, the matrix-fracture diffusivity ratio was given as

$$\chi_f = \frac{k_m}{k_f} \cdot \frac{(\varphi c)_f}{(\varphi c)_m} \sim \frac{w_{fD}}{C_{fD}}, \tag{24}$$

which was generally a large value. It was considered that the volume of the fracture was small compared with the matrix, and the transient response in the fracture reached the pseudo steady state quickly (Zeng et al., 2012). Thus, the compressibility effects in the fracture were neglected in this example.

Figure 9 displays the dimensionless drawdown field and the flux exchange. The distributions of the flow rate and the drawdown field were symmetrical to the connecting line between the wellbore and the fracture-fracture interconnection. In Region III, as shown in Figure 9a, the fluids in the matrix entered Fracture 3 through LHS3, and the exchange flow rate decreased from the fracture tip to the interconnection

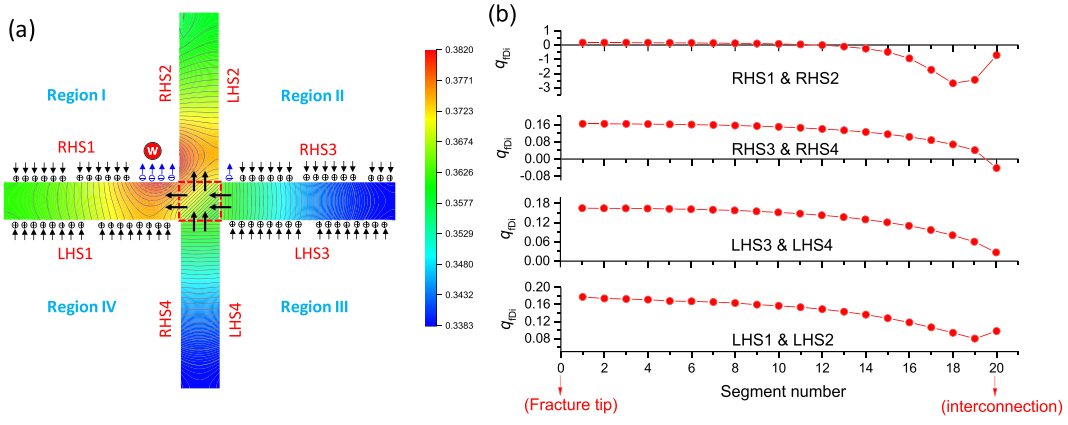

Figure 9. Flow exchange between the fracture and the matrix for the network fracture with interconnection: (a) dimensionless drawdown field within the network fractures, (b) exchange flow rate of the fracture segment ($C_{fD} = 10\pi$, $t_D = 0.1$).

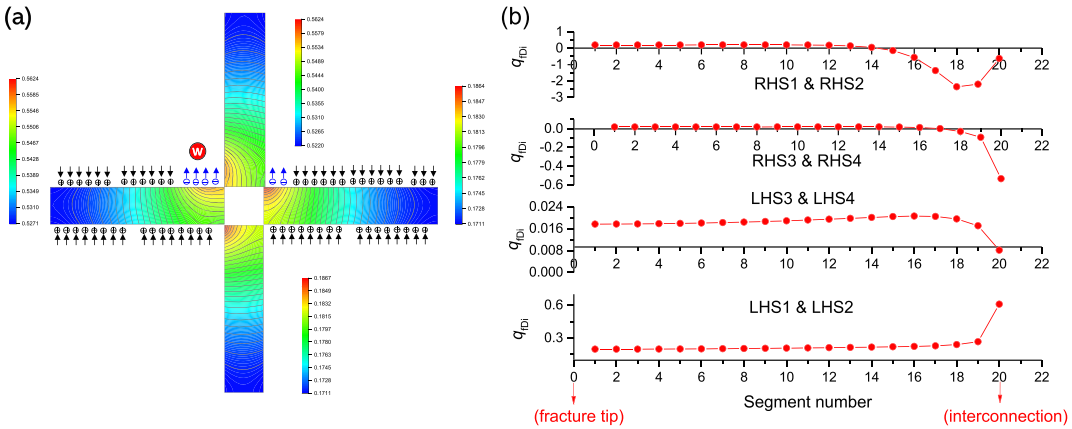

Figure 10. Flow exchange between the fracture and the matrix for the network fracture without interconnection: (a) drawdown field within the network fractures, (b) exchange flow rate of the fracture segment ($C_{fD} = 10\pi$, $t_D = 0.1$).

monotonously, which was reflected by the third plot in Figure 9b. Part of the fluids in Region II entered Fracture 3 through RHS3, and they were transmitted along Fracture 3 towards the fracture-fracture interconnection. There were two methods of conducting fluids around the interconnection. In the first methods, some fluids on the segments of RHS3 close to the interconnection (second plot in Figure 9b) outflowed from Fracture 3 and entered Region II. Afterwards, these fluids entered Fracture 2 through LHS2 (fourth plot in Figure 9b). In the second method, the rest of the fluids entered Fracture 2 through the interconnection. The rest of the fluids in Region II entered Fracture 2 directly. Thus, the flow process in Region II was diagrammatized a:

$$\text{Region II:}\left\{\underbrace{\text{RHS3}}_{\text{inflow}}\rightarrow\text{Fracture3}\rightarrow\left\{\begin{array}{l}\text{interconnection}\rightarrow\text{Fracture2}\\ \underbrace{\text{RHS3}}_{\text{outflow}}\rightarrow\text{RegionII}\rightarrow\underbrace{\text{LHS2}}_{\text{inflow}}\rightarrow\text{Fracture2.}\end{array}\right.\underbrace{\text{LHS2}}_{\text{inflow}}\rightarrow\text{Fracture2..}\right. \tag{25}$$

The fluids in Region I entered Fracture 1 through the faraway segments on RHS1, and they were then conducted towards the segments near the wellbore. Finally, all the fluids were withdrawn through the segments of Fracture 1 that were close to the wellbore on RHS1. It should be noted that because of the symmetry, the characteristics of the flow exchange in Region IV were the same as those in Region II and likewise for RHS1 versus RHS2 in Region I.

To highlight the influence of the interconnection in the continuously fractured system, Figure 10 displays the flux exchange without the interconnection. These characteristics displayed similar observations to those presented in Figure 9. The main difference was that the magnitude of the outflow on RHS3 was increased (second plot in Figure 10b) and the influx on LHS2 increased (fourth plot in Figure 10b). The reason for this was explained by the fact that all the fluids in Fracture 3 outflowed through the segments of RHS3 and were

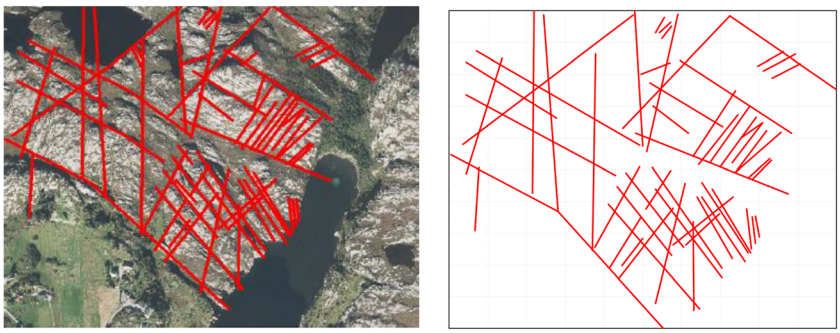

Figure 11. Fracture set in a confined aquifer modified from the work of Flemisch et al. (2017).

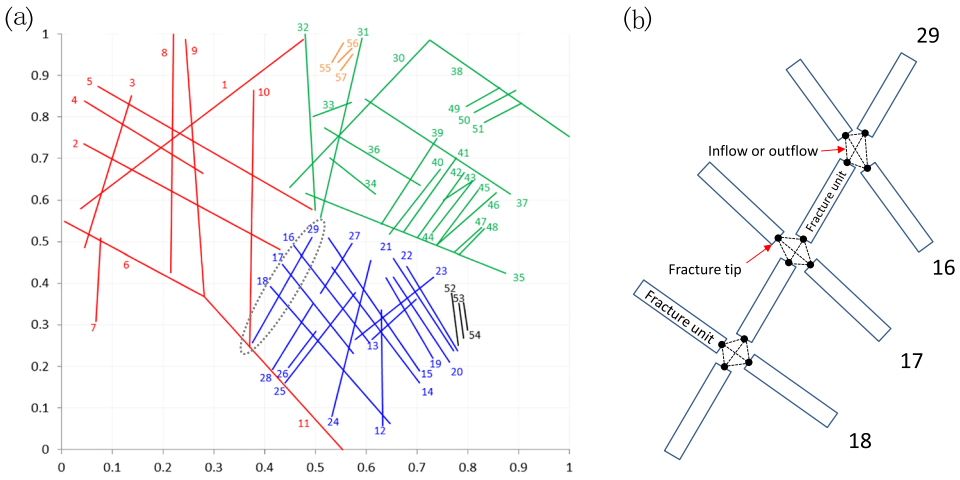

Figure 12. (a) Numbered group of the set of fractures and (b) discretization scheme of a network element.

then injected into Fracture 2 through LHS2. In other words, no fluids in Fracture 3 entered Fracture 2 through the interconnection.

It should be noted that the dimensionless drawdown in Figure 9a was higher than that in Figure 10a, which indicated that the interconnection indeed enhanced the ability of the conducting fluids for the continuous fracture network. In addition, the characteristics of the flow exchange of Fracture 1–Fracture 4 in Figures 9 and 10 were consistent with Figure 6a, so the network fractures also played the combined role of a highly conductive channel and a leaky fault when the well was located at the matrix.

3.2. Application of the Present Model to Confined Fractured Aquifers

In the real world, confined fractured aquifers are ubiquitous in a hydrogeology system. This is caused by tectonic forces, cooling stresses in magma, thermal loading, and the weathering process (Kuchuk & Biryukov, 2014; Marechal & Dewandel, 2004). If the location of a fracture was known, the fracture was deterministically presented in the model. Otherwise, the fractures were generated stochastically based on the probability distributions of the fracture length, orientation, and aperture derived from field observations. The method of fracture representation is not addressed in the present work.

To demonstrate the groundwater flow problems in a hydrogeological application, a realistic case based on an interpreted outcrop in Sotra Island presented by Flemisch et al. (2017) was introduced, with a slightly modified inner boundary condition and a computational domain. We used a pumping well as an inner boundary condition in this example. The interpreted outcrop and a more complex two-dimensional example with discrete and continuous fractures are presented in Figure 11. For simplicity, the matrix properties were assumed to be homogeneous throughout the aquifer and the fracture conductivity was assumed to be infinite for all the fractures. It is worth noting that the length of the domain size was regarded as the reference length.

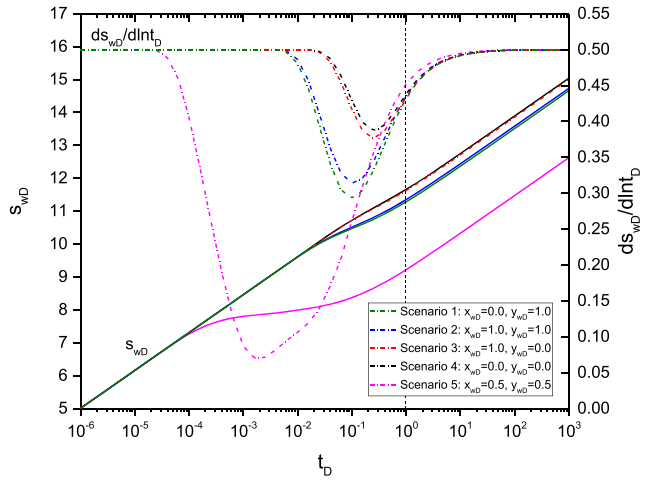

Figure 13. Effect of the location of the pumping well on the dimensionless wellbore drawdown of the aquifer when the well was in the matrix.

As shown in Figure 12a, the set was composed of 57 fractures grouped in five different subsets (denoted by different colors) according to the definition in section 2.1. Each group was not connected with the others. For the red, blue, and green groups, the fractures were interconnected in a network. Each group had a unified drawdown system. The pumping well was positioned either at the matrix or intersecting a fracture. Figure 12b shows the illustration of a network element. The element consists of four fractures (Fractures 16–18 and 29) and three interconnections. The relationships of flux exchange (outflow or inflow) among different units are

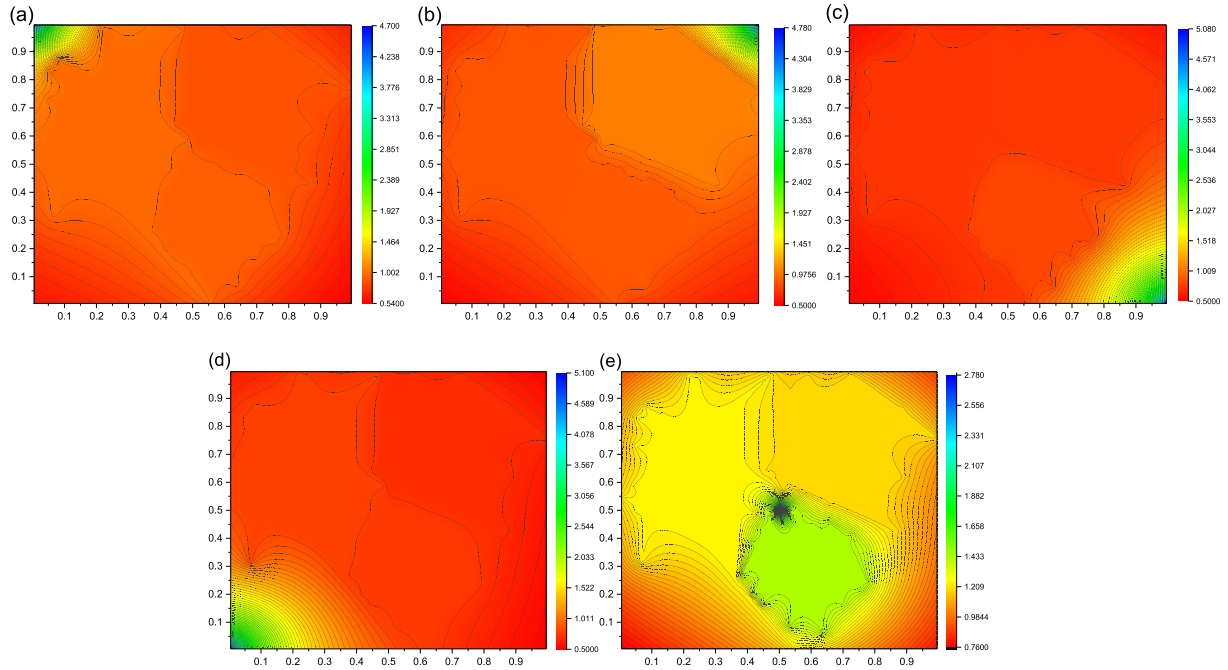

Figure 14. Representation of the drawdown field for Figure 13 when $t_D = 1$ in (a) Scenario 1, (b) Scenario 2, (c) Scenario 3, (d) Scenario 4, and (e) Scenario 5.

determined automatically based on continuous condition of drawdown and flux rate on fracture tips. Note that the interconnection in this case is regarded as a virtual one for enhancing the computation efficiency.

3.2.1. Pumping Well in the Matrix

For the first subsection, the pumping well was positioned at the matrix. We set five scenarios with different locations of the wellbore. Given the same distribution of fractures, the location of the pumping well made a significant difference in the wellbore drawdown responses. As observed in Figure 13, all the curves behaved the same way at the early times ($t_D < 10^{-4}$) before the drawdown disturbance that was generated at the wellbore reached the nearest fracture. After that, the participation of the fractures led to the decrease of the drawdown. The drawdown behaviors between Scenarios 1 and 2 were similar, as were the drawdown behaviors between Scenarios 3 and 4. However, there were noticeable differences for the drawdown derivatives between Scenarios 1 and 2, as there were in Scenarios 3 and 4. It should be noted that only one downward dip was observed on drawdown derivative curves. The reason for this was that the wellbore drawdown was mainly affected by the network fractures that were closet to well. The effect caused by other fractures was almost dissembled by the nearest network fracture. Therefore, the effects of all the fractures were shown in one dip valley. It was also noticed that the length of the nearest fracture was longer in each scenario (Scenarios 1–5). As a result, the example could not exhibit the two-valley drawdown derivative behavior.

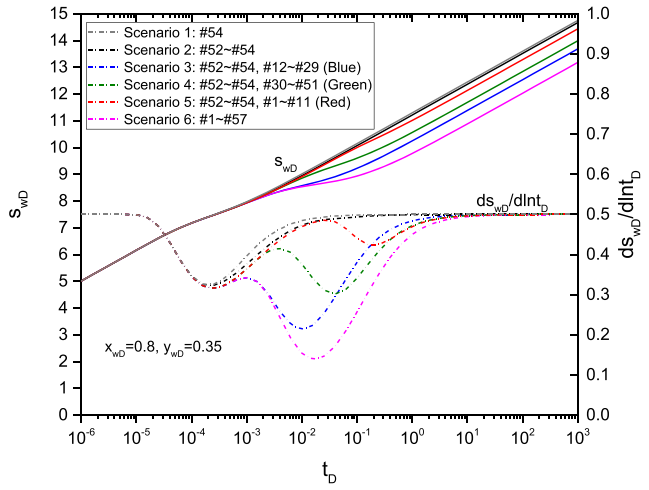

Figure 15. Effect of the location of the fracture network and the number of fractures on the dimensionless wellbore drawdown of the aquifer when the well was in the matrix.

The distributions of the hydraulic drawdown when $t_D = 1$ are shown in Figure 14. In Scenario 5, when the well was placed at $x_{wD} = 0.5$ and $y_{wD} = 0.5$, the distance between the wellbore and the nearest network fracture was the smallest. As expected, Figure 14e shows a region with a more uniformly distributed drawdown, which resulted in the lowest wellbore drawdown in Figure 13. This indicated that the drawdown disturbance arrived almost simultaneously at three groups of network fractures (i.e., red [#1–12], blue [#12–29], and green [#30–51]). In contrast, Figure 14 presents a lower wellbore drawdown in Scenarios 1 and 2,

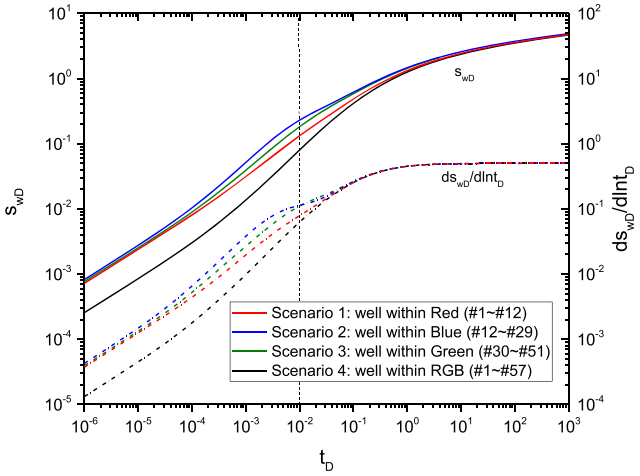

Figure 16. Effect of the location of the pumping well on the dimensionless wellbore drawdown of the aquifer when the well intersected the network fracture.

which was consistent with only one group of network fractures being employed, as shown in Figures 14a and 14b. In Scenarios 3 and 4, the distance between the wellbore and the nearest fracture was relatively larger. Hence, a larger wellbore drawdown was caused as shown in Figure 14. It was more difficult to employ any group, which was confirmed by Figures 14c and 14d.

As shown in Figure 15, the pumping well was positioned at $x_{wD} = 0.8$ and $y_{wD} = 0.35$, which was close to an isolated fracture (#54) rather than a network. The length of Fracture 54 was shorter than the other neighboring fractures. Figure 15 displays the effects of the number of fractures and the location of the fracture network on the wellbore drawdown. We assume that only one fracture (#54) existed in Scenario 1. In Scenario 1, one dip was observed on the drawdown derivative curve. When three fractures (#52–54) were considered in Scenario 2, as expected, a deeper dip of the derivative was displayed. In Scenarios 1 and 2, only one dip was observed, which was explained by the fact that the lengths of these three fractures (#52–54) were similar and the effects of all of the fractures were shown in one dip valley. In Scenario 3, it was assumed that there were 21 fractures, that is, #52–54 and #12–29 (blue group). The increase of the number of fractures led to a decrease of the drawdown. It should be noted that the average length of the blue group was longer than that of #52–54. As a result, the second dip behavior appeared as soon as the blue group fractures were felt. Similar behavior occurred in Scenarios 4–6. The degree of drawdown decrease was determined by the distance between the wellbore and the network fractures, as well as the total length of the network. Generally, the more network fractures there were, the smaller the distance was and the deeper the dip on the derivative curve was.

3.2.2. Pumping Well Intersecting Fracture

For the second subsection, the pumping well intersected either one isolated fracture or network fractures. Due to the assumption of infinite conductivity of the network, the wellbore drawdown was independent on the location of the wellbore when the pumping well intersected one of the red, blue, or green group networks. Figure 16 presents the effect of the position of the pumping well intersecting different network groups. In Scenarios 1–3, the pumping well intersected one fracture of the red (#1–12), blue (#12–29), and green (#30–51) group networks. In Scenario 4, these three groups (#1–57) were assumed to have a unified hydraulic head system. In other words, Fractures 1–57 generated a network. The wellbore drawdown was mainly affected by the total length and the density of the connected network at which the pumping well was located. The total dimensionless length of the blue group network was 4.513, the total dimensionless length of the green group network was 4.692, and the total dimensionless length of the red group network was 5.045. In addition, the configuration of the blue group network is the densest, while that of the red group network was the most sparse. Among Scenarios 1–3, the wellbore drawdown of the blue group (Scenario 2) was the largest, while the drawdown of the red group (Scenario 1) was the smallest. To highlight the effect of the fracture-fracture interconnection, three groups were assumed to be interconnected in an integrated network in Scenario 4, and the resulting wellbore drawdown was significantly decreased.

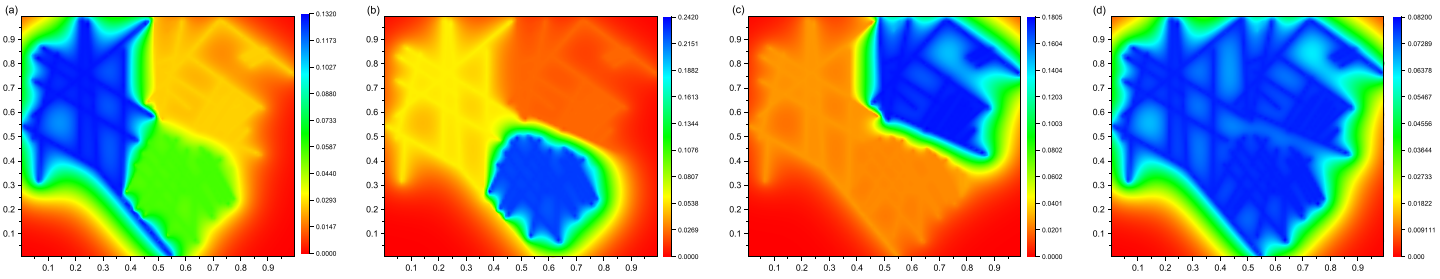

Figure 17. Representation of the drawdown field for Figure 16 when $t_D = 0.01$ for (a) Scenario 1, (b) Scenario 2, (c) Scenario 3, and (d) Scenario 4.

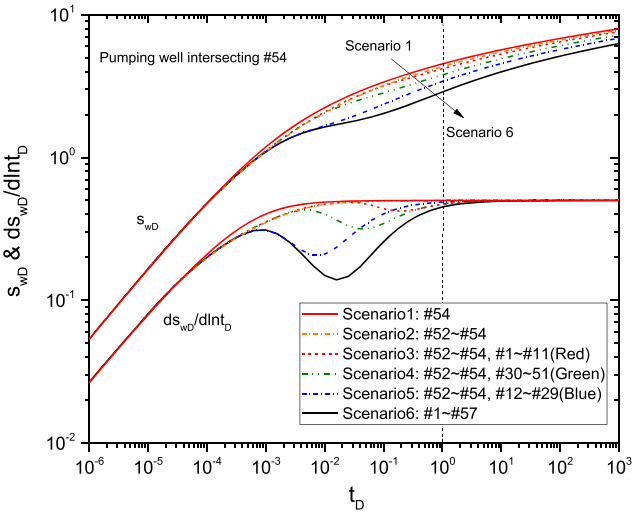

Figure 18. Effect of the location of the fracture network and the number of fractures on the dimensionless wellbore drawdown of the aquifer when the well intersected isolated fracture.

Figure 17 presents the corresponding distribution of the hydraulic drawdown when $t_D = 0.01$. For Scenarios 1–3, Figure 17a displays the fact that the red group network occupied the largest region, and a more effective communication with the blue group network was created with the help of Fracture 11. Figure 17b shows that the region occupied by the blue group network was the smallest, and the depletion of the hydraulic head was mainly concentrated in the region. Figure 17c shows that the region covered by the green group network was larger than that of the blue group network and that the interaction of the drawdown within the green group network was weaker than that of the blue group network because of the sparse configuration of the green group network. For Scenario 4 presented in Figure 17d, the entire region could be depleted due to the assumption of an integrated network. The distribution of the drawdown was more uniform.

Figure 18 presents the effect of the number of fractures and the distance between the intersected fracture and the network when the pumping well intersects Fracture 54. The corresponding field of the hydraulic drawdown is presented in Figure 19. In Scenario 1, only one fracture (#54) was assumed to exist. An integrated evolution of the drawdown behavior, which was dominated by the classical hydraulic fracture, is displayed in the figure. In Scenario 2, when three fractures (#52–54) were considered, the increase of the number of fractures contributed to a lower drawdown and derivative. Furthermore, the red, green, and blue group networks were considered throughout Scenarios 3–5. As soon as the drawdown disturbance was influenced by the network, the second valley on the derivative curve was observed. It should be noted that the total length of the network had the same order of magnitude among Scenarios 3–5. Therefore, the distance had a significant influence. In Scenario 5, since the distance between Fracture 54 and the blue group network was smallest, the wellbore drawdown was the lowest among Scenarios 3–5. Correspondingly, as shown in Figure 19c, the region covered by the blue group network could be depleted more efficiently and vice versa, as shown in Figures 19a and 19b. Therefore, the closer the network was to Fracture 54, the lower the drawdown was. In Scenario 6, when all the fractures (#1–57) were considered, the lowest drawdown was observed among Scenarios 1–6. The entire region was also depleted, as shown in Figure 19d. Hence, the more fractures there were, the lower the drawdown was. In summary, the phenomenon displayed nearly the same behavior as that presented in Figure 15.

4. Discussions: Warren-Root's Model Versus the Present Model

As shown by previous figures including Figures 13, 15, and 18, the derivatives for different scenarios exhibited some look-alike behaviors similar to the Warren and Root (1963) dual-porosity model. Of course, the model used in these figures had nothing to do with Warren and Root's physical model. According to the physical configuration of the dual-porosity model for which the well was located at the connected fracture network, flow took place in the fracture network, and the matrix blocks acted as local source elements to supply the fractures. However, the derivative curves for the case of the well intersecting fracture network

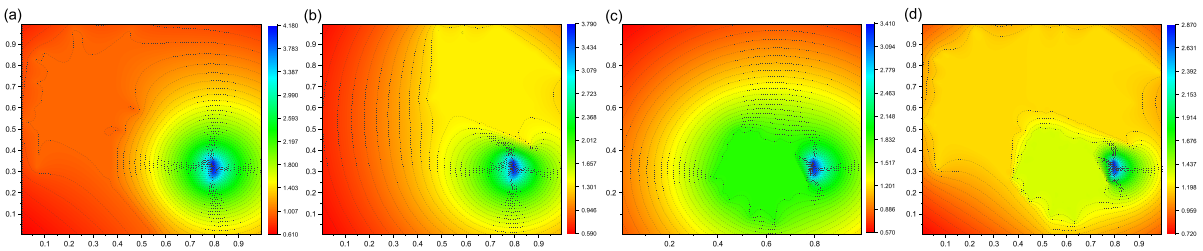

Figure 19. Representation of the drawdown field for Figure 18 when $t_D = 0.01$ in (a) Scenario 3, (b) Scenario 4, (c) Scenario 5, and (d) Scenario 6.

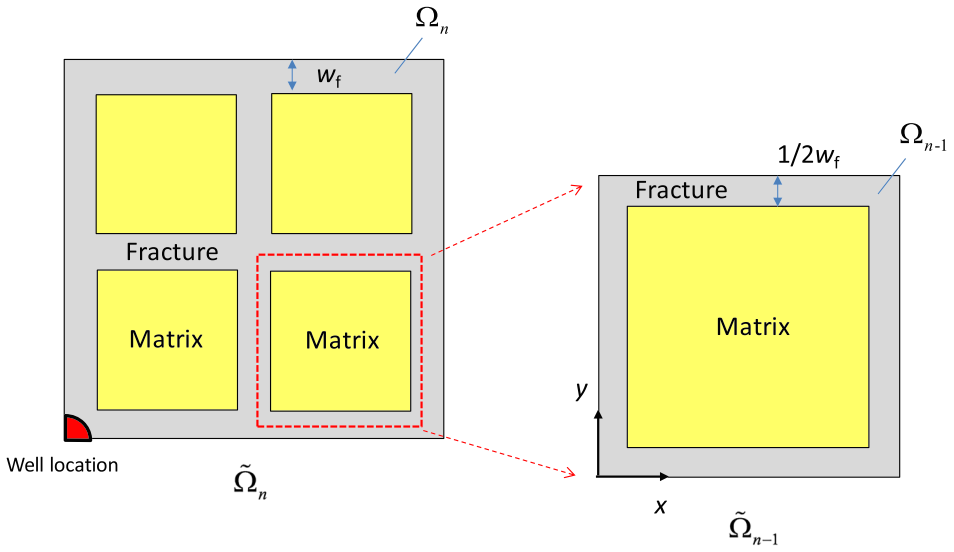

Figure 20. Schematic of a cell in the continuously fractured model with uniformly distributed fractures and matrix blocks.

(Figure 15) did not exhibit the characteristics of the Warren and Root dual-porosity model (i.e., a dip on the drawdown derivative curves). On the contrary, the cases of a well in the matrix or an intersecting isolated fracture (Figures 13, 15, and 18) exhibited dual-porosity model derivative behavior.

It should be noted that Warren and Root's dual-porosity model is a fictitious homogeneous porous medium that does not contain any fractures, while our model explicitly represented each fracture without any upscaling or homogenization, as required for dual-porosity media. To obtain the characteristics of the Warren and Root dual-porosity model, an actual model of the fractured medium was established in which the well-interconnected fractures were distributed and the well was in the fracture network. As shown in Figure 20, the ratio between the linear sizes of the submedia $\tilde{\Omega}_{n-1}$ and the media $\tilde{\Omega}_n$ was the same as the ratio for the fracture that $\tilde{\Omega}_{n-1}/\tilde{\Omega}_n$. Each cell contained a matrix block surrounded by a set of fractures. We assumed that the fracture volume had the same order of magnitude as the fracture volume. According to the dimensionless definitions in Warren and Root's model (Kuchuk & Biryukov, 2014), the relationships between the dimensionless transmissivity (λ_{fD}, λ_{mD}) and the diffusivity coefficients in our model (η_{fD}, η_{mD}) and the interporosity flow coefficient (λ) and storativity ratio (ω) in the Warren and Root dual-porosity model are given as

$$\eta_{mD} = \frac{\lambda_{mD}}{1-\omega},\ \eta_{fD} = \frac{\lambda_{fD}}{\omega};\ \omega = \frac{(\varphi Vc)_f}{(\varphi Vc)_f + (\varphi Vc)_m},\ \lambda = \alpha L_{ref}^2 \frac{k_m}{k_f}, \quad (26)$$

where $\lambda_{fD} = 1$ and $\lambda_{mD} \propto \lambda$. Thus, the compressibility effect in the fracture had to be considered for this case.

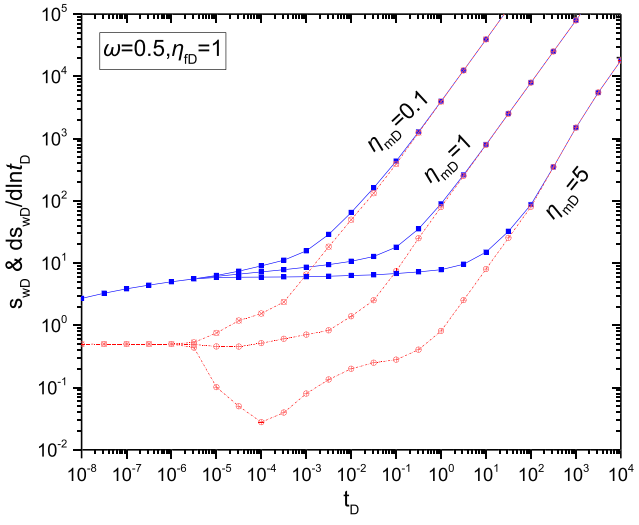

Figure 21. Dimensionless drawdown transient behavior for the continuously fractured model.

Figure 21 presents the dimensionless drawdown transient behavior for various fracture-to-matrix diffusivity ratios when $\omega = 0.5$ (i.e., when the storage capacity of the matrix was equal to the fracture). The figure illustrates the more pronounced drawdown derivative behavior similar to the Warren and Root dual-porosity model with the increase of η_{mD}. When $\eta_{mD} = 1$ (i.e., when the conductivities of the matrix and the fracture were the same), as expected, the transient drawdown was approximated to the homogeneous medium.

The drawdown field is shown in Figure 22a, where the streamlines in the matrix and fracture were in the same direction of the overall flow. When

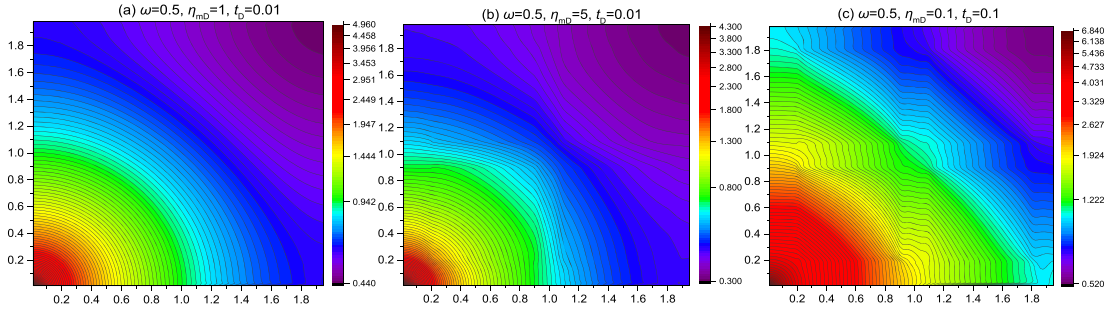

Figure 22. Flow patterns in the continuously fractured model.

$\eta_{mD} > 1$, a valley behavior similar to the characteristics of the dual-porosity model was observed on the derivative curve, which decelerated the appearance of pseudo steady state. Figure 22b plots the corresponding field. The fluids in faraway matrix blocks entered the block containing the wellbore through the fracture network, and a radial system of streamlines was generated. When $\eta_{mD} < 1$, the transient response reached the pseudo steady state (PSS) in advance, which contributed to a larger drawdown compared with the case of $\eta_{mD} = 1$. The corresponding field is plotted in Figure 22c. The streamlines in the overall flow were approximate to the pattern of radial flow, but the local streamlines in the matrix block were slightly bent towards the fractures, which indicated that the matrix began to supply the fluids towards the fractures (i.e., the characteristics of a dual-porosity model).

The phenomenon in Figure 22c was more outstanding when the matrix storage capacity was much larger than the fracture. Figure 23 displays the corresponding field, where the matrix-fracture diffusivity ratio and the storativity ratio were set to be small enough values to magnify the phenomenon. This shows that the matrix behaved like a source of fluid for the fracture. In each matrix block, the fluids flowed along the radial-shaped streamlines towards the fracture. The matrix blocks did not directly participate in the overall

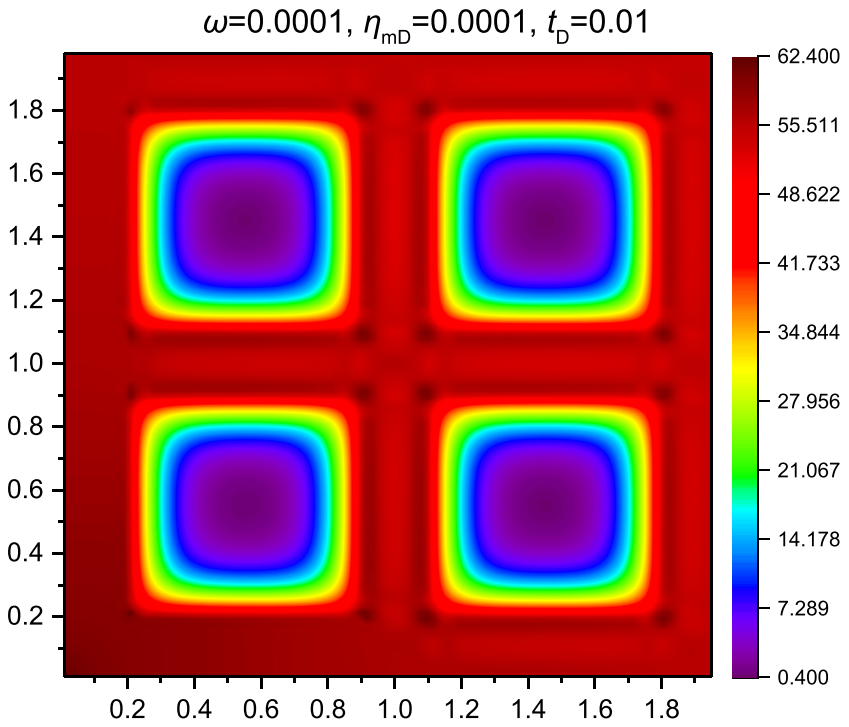

Figure 23. Flow pattern of the look-alike dual-porosity model in the continuously fractured model.

flow, and only the fractures transferred the fluids towards the wellbore. The characteristics were highly consistent with the description in the Warren and Root (1963) dual-porosity model.

5. Conclusions

With the theory of BEM and Green's function, an alternative modeling approach was developed to investigate the transient hydraulic drawdown response and the details of the flow exchange between the matrix and fracture in the discretely and continuously confined fractured aquifer. Based on this work, some important conclusions were drawn, as follows.

Although the mess-free semianalytical solution in the Laplace domain without loss of fracture properties and particularities did not require space or time discretization in the domain of interest, it allowed us to achieve the hydraulic head distribution for any spatial and temporal dimensions.

1. For the case in which the well was in the matrix, the fractures not only transmitted the fluids as a high-conductive channel, but also conducted the fluids across themselves like a leaky fault.
2. When the fracture volume was regarded as infinitesimal compared with the matrix volume, in the case of the well in the matrix, a valley was exhibited on the drawdown derivative curve in both the discretely and continuously confined fractured aquifers. However, in the case of the wellbore-intersecting fracture, the valley-like behavior was not observed unless the length of the wellbore-intersecting fracture was less than the others in the discretely fractured aquifer were.
3. When the volume of the fractures was of same order of magnitude as the matrix, in the continuously confined fractured aquifer with a uniform conductivity and fracture length, the case of the wellbore-intersecting fracture might resemble the well-known characteristics of the Warren and Root dual-porosity reservoir model.

More specifically, the characteristics of the flow exchange and the drawdown transient behavior were dependent on the fracture-matrix diffusivity ratio, the fracture-matrix capacity ratio, the fracture-matrix volume ratio, the configuration of the fracture (network), and the relative location of the wellbore. In a physical context, these parameters were of the same significance as the equivalent permeability and equivalent porosity in the equivalent homogenized model. Detailed mathematical derivations of the equivalent flow model can be found in the work of Rasoulzadeh and Kuchuk (2019).

Appendix A: Improved Green's function for equation 8

In the closed rectangular domain with the Neumann condition, the Fourier cosine transformation was used to derivate equation 8. Further using relevant mathematical relationships (Wang et al., 2018), the solution for equation 8 is given as the following equation:

$$\frac{x_{eD}\left(T_D\widetilde{G}_D\right)_\alpha}{\pi}=\frac{\cosh\left[\varepsilon_0\left(y_{eD}-|y_D\pm y_D^{'}|\right)\right]}{\varepsilon_0\sinh(\varepsilon_0 y_{eD})}+2\sum_{k=1}^{\infty}\cos(u_k x_D)\cos\left(u_k x_D^{'}\right)\frac{\cosh\left[\varepsilon_k\left(y_{eD}-|y_D\pm y_D^{'}|\right)\right]}{\varepsilon_k\sinh(\varepsilon_0 y_{eD})}, \quad \text{(A1)}$$

where we have defined

$$u_k=k\pi/x_{eD},\ \varepsilon_k=\sqrt{\nu/T_{D\alpha}+u_k^2},\ \cosh[z-|x\pm y|]=\cosh[z-|x+y|]+\cosh[z-|x-y|]. \quad \text{(A2)}$$

It should be noted that equation A1 is exact in the mathematical context. However, the components converge slowly, as if they are divergent series. Based on equation A1, we could obtain the source function on the inner and outer boundary by use of spatial integral with regard to (x'_D, y'_D). From the computational viewpoint, the integral cannot provide a solution that is convenient for computational purposes, which is difficult to terminate computations and ensure the convergence. Wang et al. (2018) provided an effective computational solution to recast the integral for fast computation. However, it is still difficult to calculate the term of $\sum\int K_0[\sqrt{\nu}f(u-\alpha)]d\alpha$ for an extremely small value of ν (corresponding to the late real time). In addition, we also encountered some other computation issues. For example, for the case of the elongated fracture, the ratio of y_{eD}/x_{eD} was very small, which made the infinite series converge slowly. Thus, the asymptotic approximations for different time scopes were developed to improve the rate of convergence.

For the late time (i.e., $v \to 0$), the transient response fully reaches the boundary-dominant state. The approximate solution of equation A1 is given by

$$\left(T_D\widetilde{G}_D\right)_\alpha = \frac{2\pi T_{D\alpha}}{x_{eD}y_{eD}v} + \frac{2\pi y_{eD}}{x_{eD}}\left(\frac{1}{3} - \frac{|y_D \pm y_D'|}{2y_{eD}} + \frac{y_D^2 + (y_D')^2}{2y_{eD}^2}\right) + 2\left(\sum_{k=1}^{\infty} H_k + \sum_{k=1}^{\infty} T_k\right). \tag{A3}$$

For an intermediate time, when the transient response is mainly affected by parallel boundaries in the x direction, equation A1 is approximated by

$$\left(T_D\widetilde{G}_D\right)_\alpha = \frac{\pi}{x_{eD}}\frac{\cosh\sqrt{v/T_{D\alpha}}(y_{eD} - |y_D \pm y_D'|)}{\sqrt{v/T_{D\alpha}}\sinh\left(\sqrt{v/T_{D\alpha}}y_{eD}\right)} + 2\left(\sum_{k=1}^{\infty} H_k + \sum_{k=1}^{\infty} T_k\right). \tag{A4}$$

When the transient response is mainly affected by parallel boundaries in the y direction, equation A1 is replaced by

$$\begin{aligned}\left(T_D\widetilde{G}_D\right)_\alpha = {} & \frac{2\pi y_{eD}}{x_{eD}}\left(\frac{1}{3} - \frac{|y_D \pm y_D'|}{2y_{eD}} + \frac{y_D^2 + (y_D')^2}{2y_{eD}^2}\right) - \frac{2\pi x_{eD}}{y_{eD}}\left(\frac{1}{3} - \frac{|x_D \pm x_D'|}{2x_{eD}} + \frac{x_D^2 + (x_D')^2}{2x_{eD}^2}\right) \\ & + \frac{\pi}{y_{eD}}\frac{\cosh\sqrt{v/T_{D\alpha}}(x_{eD} - |x_D \pm x_D'|)}{\sqrt{v/T_{D\alpha}}\sinh\left(\sqrt{v/T_{D\alpha}}x_{eD}\right)} + 2\left(\sum_{k=1}^{\infty} H_k + \sum_{k=1}^{\infty} T_k\right),\end{aligned} \tag{A5}$$

where

$$H_k = \frac{\cos(u_k x_D)\cos(u_k x_D')}{k}\left(\frac{\cosh\left[u_k(y_{eD} - |y_D \pm y_D'|)\right]}{\sinh(u_k y_{eD})} - \xi\right),\ T_k = \xi\frac{\cos(u_k x_D)\cos(u_k x_D')}{k}, \tag{A6}$$

when $y_D = y'_D = 0, \zeta = 2$; when $y_D = y'_D \neq 0, \zeta = 1$; and when $y_D \neq y'_D, \zeta = 0$. It is noted that the series of $\sum 1/k$ is not convergent. In the computation process in equations A3–A5, we first introduced the *Lobachevskiy* function to calculate the infinite series, which is given by

$$L(x) = \sum_{k=1}^{\infty}\frac{\sin(kx)}{k^2} = -\int_0^x \ln[2\sin(t/2)]dt. \tag{A7}$$

As is known, the alternate computational forms are more important than the direct analytical solution for performing an accurate numerical calculation. We believe that the observations in this study are an important contribution to the computational techniques.

Appendix B: Coefficient matrix in the linear system of equations

In equation 18, the components of the right-hand side vector are

$$\vec{B}_1^T = \left(\underbrace{0\ 0\ 0\ 0\ 0\ 0}_{\text{Block1}}\cdots\underbrace{0\ 0\ 0\ 0\ 0\ 0}_{\text{Block4}}\right) \text{and } \vec{B}_2^T = \left(\underbrace{0\ 0\ 0\ 0\ 0\ 0}_{\text{Block1}}\cdots\underbrace{0\ 0\ 0\ 0\ 0\ 1/s}_{\text{Block4}}\right). \tag{B1}$$

The coefficient sub matrixes are diagonal matrixes, as illustrated in Figure B1. The components of the coefficient matrix $\mathbf{A}_1$ are diagonal matrixes, given by

$$\mathbf{A}_1 = diag\left(\frac{\mathbf{A}_{B1}^q}{T_{D1}}, \frac{\mathbf{A}_{B2}^q}{T_{D2}}, \frac{\mathbf{A}_{B3}^q}{T_{D3}}, \frac{\mathbf{A}_{B4}^q}{T_{D4}}\right), \tag{B2}$$

where the matrix in the αth block ($\alpha = 1,2,3,4$) is expressed as follows:

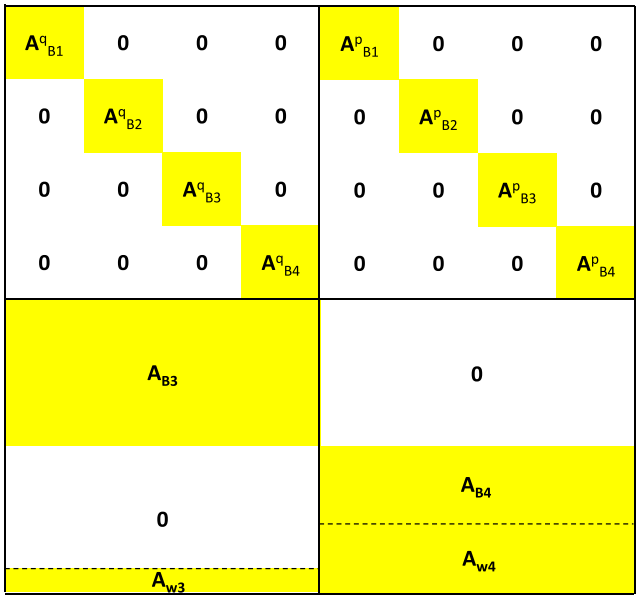

Figure B1. Coefficient matrix structure for **A**

$$\mathbf{A}_{B\alpha}^{q}=\begin{bmatrix}
\widetilde{\overline{S}}^{\alpha}_{BD(1,1;1,1)} & \widetilde{\overline{S}}^{\alpha}_{BD(1,1;1,2)} & \widetilde{\overline{S}}^{\alpha}_{BD(1,1;2,1)} & \widetilde{\overline{S}}^{\alpha}_{BD(1,1;2,2)} & \widetilde{\overline{S}}^{\alpha}_{wD(1,1;1,1)} & \widetilde{\overline{S}}^{\alpha}_{wD(1,1;1,2)} \\
\widetilde{\overline{S}}^{\alpha}_{BD(1,2;1,1)} & \widetilde{\overline{S}}^{\alpha}_{BD(1,2;1,2)} & \widetilde{\overline{S}}^{\alpha}_{BD(1,2;2,1)} & \widetilde{\overline{S}}^{\alpha}_{BD(1,2;2,2)} & \widetilde{\overline{S}}^{\alpha}_{wD(1,2;1,1)} & \widetilde{\overline{S}}^{\alpha}_{wD(1,2;1,2)} \\
\widetilde{\overline{S}}^{\alpha}_{BD(2,1;1,1)} & \widetilde{\overline{S}}^{\alpha}_{BD(2,1;1,2)} & \widetilde{\overline{S}}^{\alpha}_{BD(2,1;2,1)} & \widetilde{\overline{S}}^{\alpha}_{BD(2,1;2,2)} & \widetilde{\overline{S}}^{\alpha}_{wD(2,1;1,1)} & \widetilde{\overline{S}}^{\alpha}_{wD(2,1;1,2)} \\
\widetilde{\overline{S}}^{\alpha}_{BD(2,2;1,1)} & \widetilde{\overline{S}}^{\alpha}_{BD(2,2;1,2)} & \widetilde{\overline{S}}^{\alpha}_{BD(2,2;2,1)} & \widetilde{\overline{S}}^{\alpha}_{BD(2,2;2,2)} & \widetilde{\overline{S}}^{\alpha}_{wD(2,2;1,1)} & \widetilde{\overline{S}}^{\alpha}_{wD(2,2;1,2)} \\
\widetilde{\overline{S}}^{\alpha}_{BD[1,1;1,1]} & \widetilde{\overline{S}}^{\alpha}_{BD[1,1;1,2]} & \widetilde{\overline{S}}^{\alpha}_{BD[1,1;2,1]} & \widetilde{\overline{S}}^{\alpha}_{BD[1,1;2,2]} & \widetilde{\overline{S}}^{\alpha}_{wD[1,1;1,1]} & \widetilde{\overline{S}}^{\alpha}_{wD[1,1;1,2]} \\
\widetilde{\overline{S}}^{\alpha}_{BD[1,2;1,1]} & \widetilde{\overline{S}}^{\alpha}_{BD[1,2;1,2]} & \widetilde{\overline{S}}^{\alpha}_{BD[1,2;2,1]} & \widetilde{\overline{S}}^{\alpha}_{BD[1,2;2,2]} & \widetilde{\overline{S}}^{\alpha}_{wD[1,2;1,1]} & \widetilde{\overline{S}}^{\alpha}_{wD[1,2;1,2]}
\end{bmatrix}. \tag{B3}$$

Similarly, the coefficient matrix $\mathbf{A}_2$ is also a diagonal matrix,

$$\mathbf{A}_2 = diag\left(\mathbf{A}_{B1}^{p}, \mathbf{A}_{B2}^{p}, \mathbf{A}_{B3}^{p}, \mathbf{A}_{B4}^{p}\right), \tag{B4}$$

and

$$\mathbf{A}_{B\alpha}^{P}\begin{bmatrix}
-1 & 0 & 0 & 0 & 0 & 0 \\
0 & -1 & 0 & 0 & 0 & 0 \\
0 & 0 & -1 & 0 & 0 & 0 \\
0 & 0 & 0 & -1 & 0 & 0 \\
0 & 0 & 0 & 0 & -1 & 0 \\
0 & 0 & 0 & 0 & 0 & -1
\end{bmatrix}. \tag{B5}$$

The continuity conditions of pressure and flux at the outer boundary (i.e., the interface between adjacent blocks) satisfy the following expressions:

$$\left\{\tilde{s}^1_{BD1,j}=\tilde{s}^4_{BD1,j}\tilde{q}^1_{BD1,j}+\tilde{q}^4_{BD1,j}=0,\ \left\{\tilde{s}^1_{BD2,j}=\tilde{s}^2_{BD2,j}\tilde{q}^1_{BD2,j}+\tilde{q}^2_{BD2,j}=0,\ \left\{\tilde{s}^2_{BD1,j}=\tilde{s}^3_{BD1,j}\tilde{q}^2_{BD1,j}+\tilde{q}^3_{BD1,j}=0,\ \left\{\tilde{s}^3_{BD2,j}=\tilde{s}^4_{BD2,j}\tilde{q}^3_{BD2,j}+\tilde{q}^4_{BD2,j}=0,\ \text{for}\, j=1,\,2. \right. \right. \right. \right. \tag{B6}$$

Thus, equation B5 can also be written as a constant matrix, which is explicitly rearranged as

$$\mathbf{A}_{\mathrm{B3}}=\begin{bmatrix}
1&0&0&0&0&0&0&0&0&0&0&0&0&0&0&0&0&0&1&0&0&0&0&0\\
0&1&0&0&0&0&0&0&0&0&0&0&0&0&0&0&0&0&0&1&0&0&0&0\\
0&0&1&0&0&0&0&0&1&0&0&0&0&0&0&0&0&0&0&0&0&0&0&0\\
0&0&0&1&0&0&0&0&0&1&0&0&0&0&0&0&0&0&0&0&0&0&0&0\\
0&0&0&0&0&0&1&0&0&0&0&0&1&0&0&0&0&0&0&0&0&0&0&0\\
0&0&0&0&0&0&0&1&0&0&0&0&0&1&0&0&0&0&0&0&0&0&0&0\\
0&0&0&0&0&0&0&0&0&0&0&0&0&0&1&0&0&0&0&0&1&0&0&0\\
0&0&0&0&0&0&0&0&0&0&0&0&0&0&0&1&0&0&0&0&0&1&0&0
\end{bmatrix}, \tag{B7}$$

and

$$\mathbf{A}_{\mathrm{w3}}=[0\ 0\ 0\ 0\ 1\ 1\ 0\ 0\ 0\ 0\ 1\ 1\ 0\ 0\ 0\ 0\ 1\ 1\ 0\ 0\ 0\ 0\ 1\ 1]. \tag{B8}$$

In addition, the inner boundary was assumed to equal to the wellbore pressure, given by

$$\mathbf{A}_{\mathrm{w3}}=\begin{bmatrix}
0&0&0&0&1&0&0&0&0&0&0&0&0&0&0&0&0&0&0&0&0&0&0&0\\
0&0&0&0&0&-1&0&0&0&0&0&0&0&0&0&0&0&0&0&0&0&0&0&0\\
0&0&0&0&0&0&0&0&0&0&0&1&0&0&0&0&0&0&0&0&0&0&0&0\\
0&0&0&0&0&0&0&0&0&0&0&0&-1&0&0&0&0&0&0&0&0&0&0&0\\
0&0&0&0&0&0&0&0&0&0&0&0&0&0&0&0&1&0&0&0&0&0&0&0\\
0&0&0&0&0&0&0&0&0&0&0&0&0&0&0&0&0&-1&0&0&0&0&0&0\\
0&0&0&0&0&0&0&0&0&0&0&0&0&0&0&0&0&0&0&0&0&0&1&0\\
0&0&0&0&0&0&0&0&0&0&0&0&0&0&0&0&0&0&0&0&0&0&0&-1
\end{bmatrix}. \tag{B9}$$

Acknowledgments
This work is supported by the National Major Research Program for Science and Technology of China (2017ZX05063 and 2017ZX05037) and the National Natural Science Foundation of China (51674227).

References

Barenblatt, G. L., Zeltov, Y. P., & Kochina, I. (1960). Basic concepts in the theory of seepage of homogeneous liquids in fissured rocks. *Journal of Applied Mathematics and Mechanics*, *24*(5), 1286–1303. https://doi.org/10.1016/0021-8928(60)90107-6

Berkowitz, B. (2002). Characterizing flow and transport in fractured geological media: A review. *Advances in Water Resources*, *25*(8-12), 861–884. https://doi.org/10.1016/S0309-1708(02)00042-8

Berumen, S., Tiab, D., & Rodriguez, F. (2000). Constant rate solutions for a fractured well with an asymmetric fracture. *Journal of Petroleum Science and Engineering*, *25*, 49–58.

Biryukov, D., & Kuchuk, F. J. (2012). Transient pressure behavior of reservoirs with discrete conductive faults and fractures. *Transport in Porous Media*, *95*(1), 239–268. https://doi.org/10.1007/s11242-012-0041-x

Cinco-Ley, H., Samaniego, F., &Dominguez, N. (1976). Unsteady-state flow behavior for a well near a natural fracture (SPE-6019). Paper presented the 51st Annual Fall Technical Conference and Exhibition of the Society of Petroleum Engineers of AIME, New Orleans, 3-6 October.

Cinco-Ley, H., Samaniego, F., & Dominguez, N. (1978). Transient pressure behavior for a well with a finite-conductivity vertical fracture. *Society of Petroleum Engineers Journal*, *8*, 254–265.

Dejam, M., Hassanzadeh, H., & Chen, Z. X. (2018). Semi-analytical solution for pressure transient analysis of a hydraulically fractured vertical well in a bounded dual-porosity reservoir. *Journal of Hydrology*, *565*, 289–301. https://doi.org/10.1016/j.jhydrol.2018.08.020

Duguid, J. O., & Lee, P. Y. (1977). Flow in fractured porous media. *Water Resources Research*, *13*(3), 558–566. https://doi.org/10.1029/WR013i003p00558

Fang, H., & Zhu, J. T. (2018). Simulation of groundwater exchange between an unconfined aquifer and a discrete fracture network with laminar and turbulent flow. *Journal of Hydrology*, *562*, 468–476. https://doi.org/10.1016/j.jhydrol.2018.05.022

Fen, C. S., & Yeh, H. D. (2012). Effect of well radius on drawdown solutions obtained with Laplace transform and Green's function. *Water Resources Management*, *26*(2), 377–390. https://doi.org/10.1007/s11269-011-9922-y

Flemisch, B., Berre, I., Boon, W., Fumagalli, A., Schwenck, N., Scotti, A., et al. (2017). Benchmarks for single-phase flow in fractured porous media. *Advances in Water Resources*, *111*, 239–258.

Houseworth, J. E., Asahina, D., & Birkholzer, J. T. (2013). An analytical model for solute transport through a water-saturated single fracture and permeable rock matrix. *Water Resources Research*, *49*(10), 6317–6338. https://doi.org/10.1002/wrcr.20497

Izadi, M., & Yildiz, T. (2009). Transient flow in discretely fractured porous media. *SPE Journal*, *14*(02), 362–373. https://doi.org/10.2118/108190-PA

Jia, P., Cheng, L. S., Huang, S. J., & Wu, Y. (2016). A semi-analytical model for the flow behavior of naturally fractured formations with multi-scale fracture networks. *Journal of Hydrology*, *537*, 208–220. https://doi.org/10.1016/j.jhydrol.2016.03.022

Jia, P., Cheng, L. S., Huang, S. J., Xu, Z., Xue, Y., Cao, R., & Ding, G. (2017). A comprehensive model combining Laplace-transform finite-difference and boundary-element method for the flow behavior of a two-zone system with discrete fracture network. *Journal of Hydrology*, *511*, 453–469.

Jiang, Q. H., Yao, C., Ye, Z. Y., & Zhou, C. (2013). Seepage flow with free surface in fractured networks. *Water Resources Research*, *49*(1), 176–186. https://doi.org/10.1029/2012WR011991

Karimi-Fard, M., & Durlofsky, L. J. (2016). A general gridding, discretization, and coarsening methodology for modeling flow in porous formations with discrete geological features. *Advances in Water Resources*, *96*, 354–372. https://doi.org/10.1016/j.advwatres.2016.07.019

Kuchuk, F., & Biryukov, D. (2014). Pressure-transient behavior of continuously and discretely fractured reservoirs. *SPE Reservoir Evaluation & Engineering*, *17*(01), 82–97. https://doi.org/10.2118/158096-PA

Kuhlman, K. L., Malama, B., & Heath, J. E. (2015). Multiporosity flow in fractured low-permeability rocks. *Water Resources Research*, *51*(2), 848–860. https://doi.org/10.1002/2014WR016502

Leung, C. T., Hoch, A. R., & Zimmerman, R. W. (2012). Comparison of discrete fracture network and equivalent continuum simulations of fluid flow through two-dimensional fracture networks for the DECOVALE-2011 project. *Mineralogical Magazine*, *76*(8), 3179–3190. https://doi.org/10.1180/minmag.2012.076.8.31

Liu, R. C., Jiang, Y. J., Huang, N., & Sugimoto, S. S. (2018). Hydraulic properties of 3D crossed rock fractures by considering anistropic aperture distributions. *Advances in Geo-Engergy Research*, *2*(2), 113–121.

Luo, W. J., & Tang, C. F. (2014). Pressure-transient analysis of multiwing fractures connected to a vertical wellbore. *SPE Journal*, *20*(2), 1–14.

Luo, W. J., Tang, C. F., & Zhou, Y. F. (2019). A new fracture-unit model and its application to a Z-fold fracture. *SPE Journal*, *24*(01), 319–333. https://doi.org/10.2118/194024-PA

Luo, W. J., Tang, C. F., Zhou, Y. F., Ning, B., & Cai, J. (2018). A new semi-analytical method for calculating well productivity near discrete fractures. *Journal of Natural Gas Science and Engineering*, *57*, 216–223. https://doi.org/10.1016/j.jngse.2018.06.027

Marechal, J. C., & Dewandel, B. (2004). Use of hydraulic tests at different scales to characterize fracture network properties in the weathered-fractured layer of a hard rock aquifer. *Water Resources Research*, *40*, 1–17.

Moench, A. F. (1984). Double-porosity models for a fissured groundwater reservoir. *Water Resources Research*, *20*(7), 831–846. https://doi.org/10.1029/WR020i007p00831

Ozkan, E., & Raghavan, R. (1991). New solutions for well-test-analysis problems: Part 1 Analytical consideration. *SPE Formation Evaluation*, *6*(03), 359–368. https://doi.org/10.2118/18615-PA

Park, E., & Zhan, H. B. (2003). Hydraulics of horizontal wells in fractured shallow aquifer systems. *Journal of Hydrology*, *281*(1-2), 147–158. https://doi.org/10.1016/S0022-1694(03)00206-3

Rasoulzadeh, M., & Kuchuk, F. J. (2019). Pressure transient behavior of high-fracture-density reservoirs (dual-porosity models). *Transport in Porous Media*, Online.

Ren, F., Ma, G. W., Fan, L. F., Wang, Y., & Zhu, H. (2017). Equivalent discrete fracture networks for modeling fluid flow in highly fractured rock mass. *Engineering Geology*, *229*, 21–30. https://doi.org/10.1016/j.enggeo.2017.09.013

Roubinet, D., Dreuzy, J. R., & Tartakovsky, D. M. (2012). Semi-analytical solutions for solute transport and exchange in fractured porous media. *Water Resources Research*, *48*(W01542), 1–10.

Sedghi, M. M., Samani, N., & Barry, D. A. (2018). Semi-analytical solution of flow to a well in an unconfined-fractured aquifer system separated by an aquitard. *Journal of Hydrology*, *559*, 895–908. https://doi.org/10.1016/j.jhydrol.2018.03.012

Sedghi, M. M., & Zhan, H. B. (2019). Groundwater flow to a general well configuration in an unconfined aquifer overlying a fractured rock. *Journal of Hydrology*, *575*, 569–586. https://doi.org/10.1016/j.jhydrol.2019.05.059

Smith, L., & Schwartz, F. W. (1984). An analysis of the influence of fracture geometry on mass transport in fractured media. *Water Resources Research*, *20*(9), 1241–1252. https://doi.org/10.1029/WR020i009p01241

Stehfest, H. (1970). Numerical inversion of Laplace transforms. *Communication ACM*, *13*(1), 47–49. https://doi.org/10.1145/361953.361969

Wang, J. H., Wang, X. D., & Dong, W. X. (2017). Rate decline curves analysis of multiple-fractured horizontal wells in heterogeneous reservoirs. *Journal of Hydrology*, *553*, 527–539. https://doi.org/10.1016/j.jhydrol.2017.08.024

Wang, J. L., Jia, A. L., & Wei, Y. S. (2018). A general framework model for simulating transient response of a well with complex fracture network by use of source and Green's function. *Journal of Natural Gas Science and Engineering*, *55*, 254–275. https://doi.org/10.1016/j.jngse.2018.05.012

Wang, L., & Xue, L. (2018). A Laplace-transform boundary element model for pumping tests in irregularly shaped double-porosity aquifers. *Journal of Hydrology*, *567*, 712–720. https://doi.org/10.1016/j.jhydrol.2018.06.027

Warren, J. E., & Root, P. J. (1963). The behavior of naturally fractured reservoirs. *SPE Journal*, *3*(3), 245–255.

Xu, Y., Cavalcante Filho, J. A., Yu, W., & Sepehrnoori, K. (2017). Discrete-fracture modeling of complex hydraulic-fracture geometries in reservoir simulators. *SPE Reservoir Evaluation & Engineering*, *20*(02), 403–422. https://doi.org/10.2118/183647-PA

Xu, Y., Yu, W., & Sepehrnoori, K. (2019). Modeling dynamic behaviors of complex fractures in conventional reservoir simulators. *SPE Reservoir Evaluation & Engineering*, *22*(03), 1110–1130. https://doi.org/10.2118/194498-PA

Zeng, F. H., Zhao, G., & Liu, H. (2012). A new model for reservoirs with a discrete-fracture system. *Journal of Canadian Petroleum Technology*, *51*(02), 127–136. https://doi.org/10.2118/150627-PA

Zhou, W. T., Banerjee, R., Poe, B., Spath, J., & Thambynayagam, M. (2013). Semianalytical production simulation of complex hydraulic-fracture networks. *SPE Journal*, *19*(01), 6–18. https://doi.org/10.2118/157367-PA

Zidane, A., & Firoozabadi, A. (2014). An efficient numerical model for multicomponent compressible flow in fractured porous media. *Advances in Water Resources*, *74*, 127–147. https://doi.org/10.1016/j.advwatres.2014.08.010